# Mobility in the Sky: Performance and Mobility Analysis for Cellular-Connected UAVs

Ramy Amer, *Student Member, IEEE*, Walid Saad, *Fellow, IEEE*, and Nicola Marchetti, *Senior Member, IEEE*

***Abstract*— Providing connectivity to unmanned aerial vehicle-user equipment (UAV-UE), such as drones or flying taxis, is a major challenge for tomorrow's cellular systems. In this paper, the use of coordinated multi-point (CoMP) transmission for providing seamless connectivity to UAV-UEs is investigated. In particular, a network of clustered ground base stations (BSs) that cooperatively serve a number of UAV-UEs is considered. Two scenarios are studied: scenarios with static, hovering UAV-UEs and scenarios with mobile UAV-UEs. Under a maximum ratio transmission, a novel framework is developed and leveraged to derive upper and lower bounds on the UAV-UE coverage probability for both scenarios. Using the derived results, the effects of various system parameters such as collaboration distance, UAV-UE altitude, and UAV-UE speed on the achievable performance are studied. Results reveal that, for both static and mobile UAV-UEs, when the BS antennas are tilted downwards, the coverage probability of a high-altitude UAV-UE is upper bounded by that of ground user equipments (UEs) regardless of the transmission scheme. Moreover, for low signal-to-interference-ratio thresholds, it is shown that CoMP transmission can improve the coverage probability of UAV-UEs, e.g., from 28% under the nearest association scheme to 60% for an average of 2.5 collaborating BSs. Meanwhile, key results on mobile UAV-UEs unveil that not only the spatial displacements of UAV-UEs but also their vertical motions affect their handover rate and coverage probability. In particular, UAV-UEs that have frequent vertical movements and high direction switch rates are expected to have low handover probability and handover rate. Finally, the effect of the UAV-UE vertical movements on its coverage probability is marginal if the UAV-UE retains the same mean altitude.**

***Index Terms*— Cellular-connected UAVs, drones, CoMP transmission, 3D mobility, handover rate.**

## I. Introduction

THE past few years have witnessed a tremendous increase in the use of unmanned aerial vehicless (UAVs), popularly called drones, in many applications, such as aerial surveillance, package delivery, and even flying taxis [2] and [3]. Enabling such UAV-centric applications requires ubiquitous wireless connectivity that can be potentially provided by the pervasive wireless cellular network [4]–[6]. However, in order to operate cellular-connected UAVs using existing wireless systems, one must address a broad range of challenges that include interference mitigation, reliable communications, resource allocation, and mobility support [7]. Next, we review some of the works relevant to the cellular-connected UAV-enabled networks.

### A. State of the Art and Prior Works

Recently, there has been significant research related to the deployment of cellular-connected UAVs whereby UAVs can connect to a ground wireless cellular network to enhance their operations. However, it has been established that the dominance of line-of-sight (LoS) links makes inter-cell interference a critical issue for cellular systems with hybrid terrestrial and aerial user equipments (UEs). In this regard, extensive real-world simulations and fields trials in [7]–[10] have shown that a UAV-UE, in general, has poorer performance than a ground user equipment (UE). Due to the inherent down-tilt of base station (BS) antennas, it is found that UAVs at $40$ m and higher, will be eventually served by the side-lobes of the BS antennas, which have reduced antenna gain compared to the corresponding main-lobes. However, UAV-UEs at $40$ m and above experience favorable free-space propagation conditions. Interestingly, the work in [9] showed that the free-space propagation can make up for the BS antenna side-lobe gain reduction. However, this merit of such a favorable LoS channel that UAV-UEs enjoy vanishes at high altitudes and turns to be one of their key limiting factors. This is because the free-space propagation also leads to stronger LoS interfering signals. Eventually, UAV-UEs at high altitudes potentially exhibit poorer communication and coverage compared to ground UEs [7]–[11].

While the works in [7]–[11] explored the feasibility of providing cellular connectivity for UAVs, they did not envision new techniques to improve their performance. In particular, UAVs, at high altitudes, have limited coverage and connectivity due to the encountered LoS interference and reduced antenna gains. Moreover, their cell association will be essentially driven by the side-lobes of BS antennas, which will lead to more handovers and handover failures for mobile

Manuscript received August 12, 2019; revised December 22, 2019; accepted January 29, 2020. Date of publication February 13, 2020; date of current version May 15, 2020. This publication has emanated from research conducted with the financial support of Science Foundation Ireland (SFI) and is co-funded under the U.S. National Science Foundation under Grant CNS-1836802. This article was presented in part at the IEEE WCNC 2019 [1]. The associate editor coordinating the review of this article and approving it for publication was N. Tran. *(Corresponding author: Ramy Amer.)*

Ramy Amer and Nicola Marchetti are with CONNECT Centre for Future Networks, Trinity College Dublin, Dublin 2, D02 PN40 Ireland (e-mail: ramyr@tcd.ie; nicola.marchetti@tcd.ie).

Walid Saad is with Wireless@VT, Bradley Department of Electrical and Computer Engineering, Virginia Tech, Blacksburg, VA 24061 USA (e-mail: walids@vt.edu).

Color versions of one or more of the figures in this article are available online at http://ieeexplore.ieee.org.

Digital Object Identifier 10.1109/TCOMM.2020.2973629

UAV-UEs [9]. This necessitates the need to have sky-aware cellular networks that can seamlessly cover high altitudes UAV-UEs and support their inevitable mobility. Next, we review some recently-adopted techniques that aimed to provide reliable connectivity to the UAV-UEs.

Recently, various approaches have been proposed in [12]–[17] in order to improve the cellular connectivity for UAVs using, e.g., massive multiple-input multiple-output (MIMO), millimeter wave (mmWave), beamforming, and power control. For instance, in [12], we proposed a MIMO conjugate beamforming scheme that can improve the cellular connectivity for UAV-UEs and enhance the system spectral efficiency. Moreover, the authors in [15] incorporated directional beamforming at aerial BSs to alleviate the strong LoS interference seen by their served UAV-UEs. However, while interesting, the works in [12]–[17] only considered scenarios of static UAV-UEs. Moreover, they did not consider the use of cooperative communication through coordinated multipoint (CoMP) transmissions for UAV-UEs, which is a prominent interference mitigation tool that can diminish the effect of LoS interference. For instance, the work in [18] proposed CoMP transmissions from UAV-BSs in order to spatially multiplex signals from ground UEs and forward them to a central processor.

Unlike the static UAV assumptions in [11]–[17], the study of mobile UAVs has been conducted in [19]–[28]. Prior works in the literature followed two main directions pertaining to trajectory design for mobile UAVs. The first line of work focuses on deterministic trajectories, whereby a UAV is assumed to travel between two deterministic, possibly known, locations [19]–[21]. This type of trajectories can be used for path planning and mission-related metrics' optimization, e.g., mission time and achievable rates. For instance, the authors in [19] studied the problem of trajectory optimization for a cellular-connected UAV flying from an initial location to a final destination. Moreover, the work in [21] proposed an interference-aware path planning scheme for a network of cellular-connected UAVs based on deep reinforcement learning.

The second line of work in [22]–[25] considers stochastic trajectories in which the movements of UAVs are characterized by means of stochastic processes. This type of trajectories is usually adopted in the study of communication and mobility-related metrics such as coverage probability and handover rate. For example, in [22], the authors proposed a mixed random mobility model that characterizes the movement process of UAVs in a finite three-dimensional (3D) cylindrical region. The authors characterized the ground UE coverage probability in a network of one static serving aerial BS and multiple mobile interfering aerial BSs. The authors extended their work in [23] such that both serving and interfering aerial BSs are mobile. Meanwhile, the authors in [24] showed that an acceptable ground UE coverage can be sustained if the aerial BSs move according to certain stochastic trajectory processes. Recently, the work in [25] characterized the performance of several canonical mobility models for UAV-BSs in an infinite drone network. However, while interesting, the proposed mobility models in [22]–[24] can only describe the motions of UAV-BSs deployed in a bounded cylindrical region in space. In contrast, cellular-connected UAV-UEs such as flying taxis and delivery drones can have very long trajectories that cross multiple areas served by different BSs. Moreover, the canonical mobility models in [25] are only suitable for two-dimensional (2D) mobile UAV-BSs, while UAV-UEs are susceptible to inevitable 3D motions.

Ensuring reliable connectivity for such mobile UAV-UEs is of paramount importance for the control and operations of UAV systems. In this regard, the mobility performance of cellular-connected UAVs has been studied in recent works [26]–[28]. In [26], the authors quantified the impact of handover on the UAV-UE throughput, assuming that no payload data is received during the handover procedures. Meanwhile, in [27], based on system-level simulations, it is revealed that high handover rate is encountered when the UAV-UE moves through the nulls between side-lobes of the BS antennas. Moreover, based on experimental trials, in [28], the authors showed that under the strongest received power association, drones are subject to frequent handovers once the typical flying altitude is reached. However, the results presented in these works are based on simulations and measurements.

While there exist some approaches in the literature to improve the cellular connectivity for UAV-UEs [12]–[17], none of these works studied the role of CoMP transmission as an effective interference mitigation tool to support the UAV-UEs. Moreover, these works only considered scenarios of static UAV-UEs. Furthermore, while the authors in [26]–[28] studied the performance of mobile UAV-UEs, their results were based on system simulations and measurement trials. Particularly, a rigorous analysis for mobile UAV-UEs to quantify important performance metrics such as coverage probability and handover rate is still lacking in the current state-of-the-art. *To our best knowledge, this paper provides the first rigorous analysis of CoMP transmission for both static and 3D mobile UAV-UEs, where a novel 3D mobility model is also provided.*

### B. Contributions

The main contribution of this paper is a novel framework that leverages CoMP transmissions for serving cellular-connected UAVs, and develops a novel mobility model that effectively captures the 3D movements of UAV-UEs. We propose a maximum ratio transmission (MRT) scheme aiming to maximize the desired signal at the intended UAV-UE, and, hence, the performance of cellular communication links for the UAV-UEs can be improved. In particular, we consider a network of disjoint clusters in which BSs in one cluster collaboratively serve one UAV-UE within the same cluster via coherent CoMP transmission. For this network, we consider two key scenarios, namely, static and mobile UAV-UEs. Using Cauchy's inequality and Gamma approximations, we develop a novel framework that is then leveraged to derive tight upper bound (UB) and lower bound (LB) on the UAV-UE coverage probability for both scenarios. Moreover, for mobile UAV-UEs, we analytically characterize the handover rate, and handover probability based on a novel 3D mobility model. We further

quantify the negative impact of the UAV-UEs' mobility on their achievable performance.

Our results reveal that the achievable performance of UAV-UEs heavily depends on the UAV-UE altitude, UAV-UE speed, and the collaboration distance, i.e., the distance within which the UAV-UE is cooperatively served from ground BSs. Moreover, while allowing CoMP transmission substantially improves the UAV-UEs' performance, it is shown that their performance is still upper bounded by that of ground UEs due to the down-tilt of the BS antennas and the encountered LoS interference. Additionally, results on mobile UAV-UEs unveil that the spatial displacements of UAV-UEs jointly with their vertical motions affect their handover rate and handover probability. Moreover, while the UAV-UE spatial movements considerably impact its coverage probability (due to handover), the effect of the UAV-UE vertical displacements is marginal if the UAV-UE fluctuates around the same mean altitude. *Overall, cooperative transmission is shown to be particularly effective for high altitude UAV-UEs that are susceptible to adverse interference conditions, which is the case in a variety of drone applications.*

The rest of this paper is organized as follows. Section II and Section III present, respectively, the system model and the coverage probability analysis for static UAV-UEs. Section IV develops a novel 3D mobility model and Section V studies the performance of 3D mobile UAV-UEs. Numerical results are presented in Section VI and conclusions are drawn in Section VII.

## II. System Model

We consider a terrestrial cellular network in which BSs are distributed according to a 2D homogeneous Poisson point process (PPP) $\Phi_b = \{b_i \in \mathbb{R}^2, \forall i \in \mathbb{N}^+\}$ with intensity $\lambda_b$. All BSs have the same transmit power $P_t$, and are deployed at the same height $h_{\mathrm{BS}}$. We consider a number of high altitude cellular-connected UAV-UEs that can be either static or mobile based on the application. Particularly, the UAV-UEs are either hovering or moving at altitudes higher than the BS heights. We consider a cluster-centric UAV-UE model in which BSs are grouped into disjoint clusters modeled using a hexagonal grid with an inter-cluster center distance equal to $2R_h$, see Fig. 1. The area of each cluster is hence given by $A = 2\sqrt{3}R_h^2$. For analytical convenience, we approximate the cluster area to a circle with the same area, i.e., with collaboration distance $R_c$ where $\pi R_c^2 = 2\sqrt{3}R_h^2$, and $R_c = \sqrt{\frac{2\sqrt{3}}{\pi}}R_h$. *BSs belonging to the same cluster can cooperate to serve one UAV-UE within their cluster so as to mitigate the effect of LoS interference and, hence, enhance the UAV-UE cellular connectivity.*

### A. Channel Model

We consider a wireless channel that is characterized by both large-scale and small-scale fading. For the large-scale fading, the channel between BS $i$ and an arbitrary UAV-UE is described by the LoS and non-line-of-sight (NLoS) components, which are considered separately along with their probabilities of occurrence [29]. This assumption is apropos for such ground-to-air (GTA) channels that often exhibit LoS communication (e.g., see [11] and [30]).

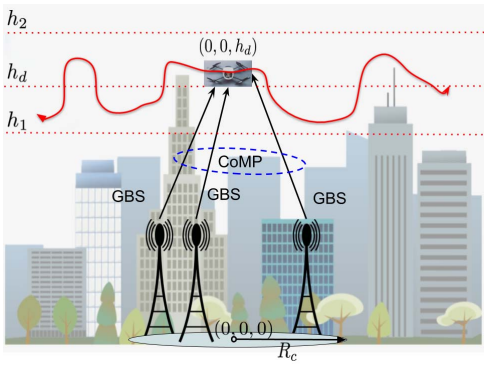


(a) Illustration of cooperative transmission

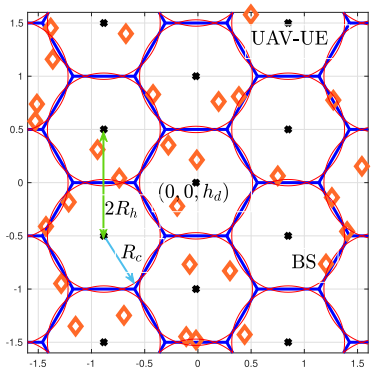


(b) Snapshot of a cluster-centric UAV-UE topology

Fig. 1. Illustration of the proposed system model where BSs cooperatively serve high-altitude UAV-UEs via CoMP transmission. UAV-UEs can be either hovering at a fixed altitude $h_d$ or flying within minimum and maximum altitudes $h_1$ and $h_2$, respectively. In (b), the clusters are defined by a hexagonal grid, wherein BSs (orange diamonds) are distributed according to a homogeneous PPP and the UAV-UEs (black stars) are hovering above the centers of disjoint clusters.

For small-scale fading, we adopt a Nakagami-$m_v$ model as done in [11] for the channel gain, whose probability distribution function (PDF) is given by: $f(\omega) = \frac{2m_v^{m_v}\omega^{2m_v-1}}{\Gamma(m_v)}e^{-m_v\omega^2}$, where $m_v$, $v \in \{l, n\}$, is the fading parameter which is assumed to be an integer for analytical tractability, with $m_l > m_n$. In the special case when $m_n = 1$, Rayleigh fading is recovered with an exponentially distributed instantaneous power, which can be used for the performance evaluation of ground UEs. Given that $\omega \sim \mathrm{Nakagami}(m_v)$, it directly follows that the channel gain power $\chi = \omega^2 \sim \mathrm{Gamma}(m_v, 1/m_v)$, where $\mathrm{Gamma}(K, \theta)$ is the Gamma distribution with $K$ and $\theta$ denoting the shape and scale parameters, respectively. Hence, the PDF of channel power gain distribution will be: $f_{\mathrm{X}}(\chi) = \frac{m_v^{m_v}\chi^{m_v-1}}{\Gamma(m_v)}e^{-m_v\chi}$, where $\Gamma(.)$ is the Gamma function.

3D blockage is characterized by the fraction $a$ of the total land area occupied by buildings, the mean number of buildings $\eta$ per $\mathrm{km}^2$, and the height of buildings modeled by a Rayleigh PDF with a scale parameter $c$. Hence, the probability of having

a LoS communication from a BS at horizontal-distance $r_i$ from an arbitrary UAV-UE is given, similar to [26] and [30], as:

$$\mathbb{P}_l(r_i) = \prod_{t=0}^{\lfloor \frac{r_i\sqrt{a\eta}}{1000}-1 \rfloor} \left[1 - \exp\Big( - \frac{\big(h_{\rm BS} + \frac{h(n+0.5)}{m+1}\big)^2}{2c^2}\Big)\right], \quad (1)$$

where $h$ represents the difference between the UAV-UE altitude and BS height, which depends on whether the UAV-UE is static or mobile. Different terrain structures and environments can be considered by varying the tuple $(a, \eta, c)$.

We consider typical ground BSs equipped with down-tilted antennas to account for the coverage of ground UEs that co-exist with the UAV-UEs. In particular, we assume that the antenna radiation pattern of the ground BSs is vertically directional and horizontally omnidirectional. Under such a setup, the high-altitude UAV-UEs always receive signals from the side-lobes of BS antennas [9]. For the antenna gain, we adopt a simplified rectangular model, with $G_m$ and $G_s$ being the main-lobe and side-lobe gains, respectively. This antenna model is known to provide useful performance bounds and insights on drone operations, see, e.g., [12], [26], and [30]. This model can be also considered as a variant of the idealized parabolic antenna pattern that has been recently used in 3GPP studies related to drone networks [31].

As previously discussed, the performance of relatively high-altitude UAV-UEs is limited by the LoS interference they encounter and reduced serving antenna gain (from the antennas' side-lobes [9]). We hence propose a multi-BS cooperative transmission scheme that mitigates inter-cell interference and, thus, improves the performance of high-altitude UAV-UEs. Hence, the antenna gain plus path loss for each component, i.e., LoS and NLoS, will be

$$\zeta_v(r_i) = A_v G_s d_i^{-\alpha_v} = A_v G_s \big(r_i^2 + h^2\big)^{-\alpha_v/2}, \quad (2)$$

where $d_i$ is the communication link distance, $v \in \{l, n\}$, $l$ and $n$ refer respectively to the LoS and NLoS communications, and $\alpha_l$ and $\alpha_n$ are the path loss exponents for the LoS and NLoS links, respectively. Similarly, $A_l$ and $A_n$ are the path loss constants at the reference distance $d_i = 1\text{m}$ for the LoS and NLoS, respectively.

Having defined our system model, next, we will consider two scenarios: Static UAV-UEs and mobile UAV-UEs. For each scenario, we will characterize the coverage probability of high altitude UAV-UEs that are collaboratively served from BSs within their cluster. The performance of collaboratively-served UAV-UEs is then compared to their terrestrial counterparts and to UAV-UEs under the nearest association scheme. Moreover, we will characterize the handover rate for mobile UAV-UEs and quantify the negative impact of mobility on their achievable performance. For the reader's convenience, Table I summarizes our commonly-used notations hereinafter.

TABLE I
MATHEMATICAL NOTATIONS

| Description | Notation |
|---|---|
| LoS and NLoS path-loss exponents | $\alpha_l$, $\alpha_n$ |
| LoS/NLoS path-loss constants | $A_l$, $A_n$ |
| Nakagami LoS/NLoS fading parameters | $m_l$, $m_n$ |
| UAV-UE 3D cylindrical displacement | $\boldsymbol{X}_t$ |
| UAV-UE velocity at epoch $t$ | $V_t$ |
| UAV-UE 3D transition length | $U_t$ |
| UAV-UE 2D transition length | $\rho_t$ |
| Mobility parameter | $\mu$ |
| UAV-UE average speed | $\bar{\nu}$ |
| Vertical displacement | $Z_t$ |
| Probability of handover | $\mathbb{P}(H)$ |
| SIR threshold | $\vartheta$ |
| BSs' intensity | $\lambda_b$ |
| Inter-cluster center and collaboration distances | $2R_h$, $R_c$ |
| Antenna main and side-lobe gains | $G_m$, $G_s$ |
| Gamma shape and scale parameters | $K$, $\theta$ |
| BS antenna height | $h_{\rm BS}$ |
| UAV-UE hovering altitude | $h_d$ |
| UAV-UE upper and lower altitudes | $h_1$, $h_2$ |
| Handover rate | $H$ |
| Handover cost | $\beta$ |
| Mean altitude of mobile UAV-UEs | $\mathbb{E}[Z_\infty]$ |

## III. COVERAGE PROBABILITY OF STATIC UAV-UES

Hovering drones can provide appealing solutions for a wide range of applications such as traffic control and surveillance [32]. We here assume static UAV-UEs that hover at a fixed altitude $h_d$, where $h_d > h_{\rm BS}$. Hence, we set $h = h_d - h_{\rm BS}$ in (1) and (2). We also assume that BSs within one cluster cooperatively serve one UAV-UE whose projection on the ground is at the cluster center. Note that assuming such a cluster-center UAV-UE is mainly done for tractability, but its performance can be seen as an UB on the performance of a randomly located UAV-UE inside the cluster [33]. Given that a PPP is translation invariant with respect to the origin, for simplicity, we conduct the coverage analysis for a UAV-UE located at the origin in $\mathbb{R}^2$, referred to as the *typical UAV-UE* [34]. Next, we first characterize the serving distance distribution, and then, we employ it to derive upper and lower bounds on the coverage probability of static UAV-UEs.

### A. Serving Distance Distributions

Under the condition of having $\kappa$ serving BSs in the cluster of interest, the distribution of in-cluster BSs will follow a binomial point process (BPP) [34]. This BPP consists of $\kappa$ uniformly and independently distributed BSs in the cluster. The set of cooperative BSs is defined as $\Phi_c = \{b_i \in \Phi_b \cap \mathcal{B}(0, R_c)\}$, where $\mathcal{B}(0, R_c)$ denotes the ball centered at the origin $(0,0) \in \mathbb{R}^2$ with radius $R_c$. Recall that the typical UAV-UE is located at the origin in $\mathbb{R}^2$, i.e., $(0,0,h_d) \in \mathbb{R}^3$. The 2D distances from the cooperative BSs to the typical UAV-UE are represented by $\boldsymbol{R}_\kappa = [R_1, \ldots, R_\kappa]$. Then, conditioning on $\boldsymbol{R}_\kappa = \boldsymbol{r}_\kappa$, where $\boldsymbol{r}_\kappa = [r_1, \ldots, r_\kappa]$, the joint PDF of the serving distances is $f_{\boldsymbol{R}_\kappa}(\boldsymbol{r}_\kappa)$. The $\kappa$ cooperative BSs can be seen as the $\kappa$-closest BSs to the cluster center from the PPP $\Phi_b$. Since the $\kappa$ BSs are independently and uniformly distributed in the cluster approximated by $\mathcal{B}(0, R_c)$, the PDF of the horizontal distance from the origin to BS $i$ will be: $f_{R_i}(r_i) = \frac{2r_i}{R_c^2}$, $0 \le r_i \le R_c$, for any $i \in \mathcal{K}_f = \{1, \ldots, \kappa\}$, where $\mathcal{K}_f$ is the set of collaborative BSs within $\mathcal{B}(0, R_c)$. From the independently and identically distributed (i.i.d.) property of BPP, the joint PDF of the serving distances $\boldsymbol{R}_\kappa = [R_1, \ldots, R_\kappa]$ is expressed as $f_{\boldsymbol{R}_\kappa}(\boldsymbol{r}_\kappa) = \prod_{i=0}^{\kappa} \frac{2r_i}{R_c^2}$.

### *B. Performance of UAV-UEs*

Under the condition of having $\kappa$ serving BSs, the received signal at the UAV-UE will be:

$$P = \underbrace{\sum_{i=1}^{\kappa} P_v(r_i)\omega_i w_i Y_0}_{\text{desired signal}} + \underbrace{\sum_{j\in\Phi_b\setminus\mathcal{B}(0,R_c)} P_v(u_j)\omega_j w_j Y_j}_{\text{interference}} + Z, \tag{3}$$

where the first term represents the desired signal from $\kappa$ collaborative BSs with $P_v^2(r_i) = P_t\zeta_v(r_i)$, $v \in \{l, n\}$, $\omega_i$ being the Nakagami-$m_v$ fading variable of the channel from BS $i$ to the UAV-UE, $w_i$ is the precoder used by BS $i$, and $Y_0$ is the channel input symbol that is sent by the cooperating BSs. The second term represents the inter-cluster interference, whose power is denoted as $I_{\text{out}}$, where $Y_j$ is the transmitted symbol from interfering BS $j$ and $u_j$ is the horizontal distance between interfering BS $j$ and the UAV-UE; $Z$ is a circular-symmetric zero-mean complex Gaussian random variable (RV) that models the background thermal noise. Note that $Y_j$ is a common message from multiple ground BSs $j \in \Phi_b\setminus\mathcal{B}(0, R_c)$ that are located in the same (remote) cluster.

As discussed earlier, UAV-UEs exhibit a LoS component which becomes dominant at relatively high altitudes. The LoS probability in (1) represents a delta function that goes from one to zero as $r_i$ increases. This implies that the probability of LoS communication from close BSs is higher than that of remote BSs. Hence, we consider that the desired signal is dominated by its LoS component where $v = l$, $m_v = m_l$, and $P_v(r_i) = \sqrt{P_t}\zeta_l(r_i)^{0.5}$. However, for the interfering signal, both LoS and NLoS components exist and, thus, we have: $P_v(u_j) = \sqrt{P_t}\zeta_v(u_j)^{0.5}$, $v \in \{l, n\}$. This is due to the fact that, as the LoS probability decreases with the interfering distance $u_j$, the LoS assumption becomes less practical for far but interfering BSs.

Since the cost associated with launching UAV-UEs can be high and their number is much smaller than ground UEs, it is practical to assign unique (non-reusable) training pilots for UAV-UEs. This would help avoid pilot contamination for UAV-UEs that are typically prone to poor communication channel conditions. Under this setup, the channel state information (CSI) will be available at the serving BSs, and MRT can be adopted to maximize the received power at the UAV-UEs. For MRT, we set the precoder $w_i$ as $w_i = \frac{\omega_i^*}{|\omega_i|}$, where $\omega_i^*$ is the complex conjugate of $\omega_i$ [12] and [35]. Assuming that $Y_0$ and $Y_k$ in (3) are independent zero-mean RVs of unit variance, and neglecting the thermal noise, the conditional SIR at the typical UAV-UE will be:

$$\Upsilon_{|\boldsymbol{r}_\kappa} = \frac{P_t\left|\sum_{i=1}^{\kappa}\zeta_l^{1/2}(r_i)w_i\omega_i\right|^2}{\sum_{k\in\Phi_b\setminus\mathcal{B}(0,R_c)}\left|P_v(u_k)\omega_k w_k\right|^2}, \tag{4}$$

where $\Upsilon_{|\boldsymbol{r}_\kappa}$ is conditioned on the number of collaborative BSs $\kappa$, and on $\boldsymbol{R}_\kappa = \boldsymbol{r}_\kappa$. In (4), we have $\left|\sum_{i=1}^{\kappa}\zeta_l^{1/2}(r_i)w_i\omega_i\right|^2$ representing the square of a weighted sum of $\kappa$ Nakagami-$m_l$ RVs. Since there is no known closed-form expression for a weighted sum of Nakagami-$m_l$ RVs, we use the Cauchy-Schwarz's inequality to get an UB on a square of weighted sum as follows:

$$\left|\sum_{i=1}^{\kappa}\zeta_l^{1/2}(r_i)w_i\omega_i\right|^2 = \left|\sum_{i=1}^{\kappa}\zeta_l^{1/2}(r_i)\frac{\omega_i^*\omega_i}{|\omega_i|}\right|^2 = \left(\sum_{i=1}^{\kappa}Q_i\right)^2 \le \kappa\left(\sum_{i=1}^{\kappa}Q_i^2\right), \tag{5}$$

where $Q_i = \zeta_l^{1/2}(r_i)\frac{\omega_i^*\omega_i}{|\omega_i|} = \zeta_l^{1/2}(r_i)\frac{|\omega_i|^2}{|\omega_i|} = \zeta_l^{1/2}(r_i)|\omega_i|$ is a scaled Nakagami-$m_l$ RV, and $i \in \mathcal{K}_f$. Since $\omega_i \sim \text{Nakagami}(m_l)$, from the scaling property of the Gamma PDF, $Q_i^2 \sim \text{Gamma}\big(K_i = m_l, \theta_i = \zeta_l(r_i)/m_l\big)$. To get a tractable statistical equivalence of a sum of $\kappa$ Gamma RVs with different scale parameters $\theta_i$, we adopt the method of second-order moment matching for Gamma RVs proposed in [36, Proposition 8]. It is shown that the equivalent Gamma distribution, denoted as $J \sim \text{Gamma}(K, \theta)$, with the same first and second-order moments has the following parameters:

$$K = \frac{\left(\sum_i K_i\theta_i\right)^2}{\sum_i K_i\theta_i^2} = \frac{m_l\left(\sum_i \zeta_l(r_i)\right)^2}{\sum_i\left(\zeta_l(r_i)\right)^2} \tag{6}$$

$$\theta = \frac{\sum_i K_i\theta_i^2}{\sum_i K_i\theta_i} = \frac{\sum_i \zeta_l(r_i)^2}{m_l\sum_i\zeta_l(r_i)}. \tag{7}$$

To showcase the accuracy of the second-order moment approximation in our case, for an arbitrary realization of the network, we plot in Fig. 2 the PDF of the equivalent channel gain. As evident from the plot, approximating a sum of $\kappa$ Gamma RVs with an equivalent Gamma RV, whose shape and scale parameters are respectively $K$ and $\theta$ from (6), is quite accurate. For tractability, we further upper bound the shape parameter $K$ using the Cauchy-Schwarz's inequality as: $K \le \frac{m_l\kappa\sum_i\left(\zeta_l(r_i)\right)^2}{\sum_i\left(\zeta_l(r_i)\right)^2} = m_l\kappa$, where, by definition, $m_l\kappa$ is integer. We shall also see shortly the tightness of this UB.

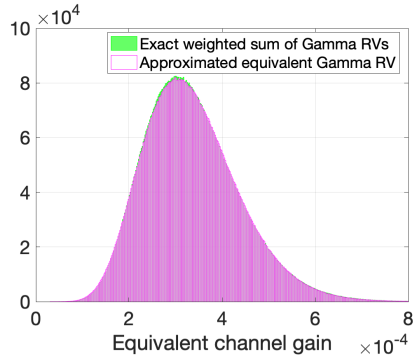


Fig. 2. Monte Carlo simulation of the PDF of the equivalent gain of channels between cooperating SBSs and the UAV-UE, including path loss and fading. A PPP realization of density $\lambda_b = 20$ per km$^2$ is run for a simulated area of 20 km$^2$ with $m_l = 3$ and $R_c = 200$ m.

Next, we derive UB and LB expressions on the UAV-UE coverage probability. Our developed approach is novel in the sense that it adopts the Cauchy-Schwarz's inequality and moment match of Gamma RVs to derive an UB on the coverage probability, which is difficult to obtain exactly.

A bound on the UAV-UE coverage probability conditioned on $\boldsymbol{R}_\kappa = \boldsymbol{r}_\kappa$ is expressed as:

$$\mathbb{P}_{\mathrm{c}|\boldsymbol{r}_\kappa} \overset{(a)}{\leq} \mathbb{P}\Big(\frac{\kappa P_t \big(\sum_{i=1}^{\kappa} Q_i\big)^2}{I_{\mathrm{out}}} > \vartheta\Big) \overset{(b)}{\approx} \mathbb{P}\Big(\frac{\kappa P_t J}{I_{\mathrm{out}}} > \vartheta\Big), \quad (8)$$

where (a) follows from the Cauchy-Schwarz's inequality, (b) follows from the Gamma approximation and rounding the shape parameter $K = m_l\kappa$, and $\vartheta$ is the SIR threshold. The coverage probability can be obtained as a function of the system parameters, particularly, the Nakagami fading parameter and collaboration distance, as stated formally in the following theorem.

*Theorem 1: An UB on the coverage probability of UAV-UEs cooperatively served from BSs within a collaboration distance $R_c$ can be derived as follows:*

$$\mathbb{P}_{\mathrm{c}} = \sum_{\kappa=1}^{\infty} \mathbb{P}_\kappa \int_{\boldsymbol{r}_{\boldsymbol{\kappa}}=\boldsymbol{R}_{\boldsymbol{c}}}^{\infty} \mathbb{P}^l_{\mathrm{c}|\boldsymbol{r}_\kappa} \prod_{i=0}^{\kappa} \frac{2r_i}{R_c^2} \mathrm{d}\boldsymbol{r}_\kappa, \quad (9)$$

*where $\mathbb{P}_\kappa = \frac{(2\sqrt{3}R_h^2\lambda_b)^\kappa e^{-2\sqrt{3}R_h^2\lambda_b}}{\kappa!}$ is the probability that there are $\kappa$ in-cluster collaborating BSs. The conditional coverage probability is given by $\mathbb{P}^l_{\mathrm{c}|\boldsymbol{r}} = \|e^{\boldsymbol{T}_K}\|_1$, where $\|.\|_1$ represents the induced $\ell_1$ norm and $\boldsymbol{T}_K$ is the lower triangular Toeplitz matrix:*

$$\boldsymbol{T}_K = \begin{bmatrix} t_0 & & & \\ t_1 & t_0 & & \\ \vdots & \vdots & \ddots & \\ t_{K-1} & \dots & t_1 & t_0; \end{bmatrix}$$

*$K = m_l\kappa$, $t_i = \frac{(-\varpi)^i}{(i)!}\Omega^{(i)}(\varpi)$, $\Omega^{(i)}(\varpi) = \frac{d^i}{d\varpi^i}\Omega(\varpi)_{|\boldsymbol{r}_\kappa}$, $\Omega(\varpi)_{|\boldsymbol{r}_\kappa} = -2\pi\lambda_b \int_{\upsilon=R_c}^{\infty} \Big(1 - \delta_l \mathbb{P}_l(\upsilon) - \delta_n \mathbb{P}_n(\upsilon)\Big)\upsilon \mathrm{d}\upsilon$, $\delta_l = \Big(1 + \frac{\varpi P_l(\upsilon)^2}{m_l}\Big)^{-m_l}$, $\delta_n = \Big(1 + \frac{\varpi P_n(\upsilon)^2}{m_n}\Big)^{-m_n}$, and $\varpi = \vartheta \big/ \kappa P_t \theta$.*

*Proof:* Please see Appendix A.[1] □

The main steps towards tractable coverage are summarized as follows [37]: We first derive the conditional log-Laplace transform $\Omega(\varpi)_{|\boldsymbol{r}_\kappa}$ of the aggregate interference. Then, we calculate the $i$-th derivative of $\Omega(\varpi)_{|\boldsymbol{r}_\kappa}$ to populate the entries $t_i$ of the lower triangular Toeplitz matrix $\boldsymbol{T}_K$. The conditional coverage probability can be then computed from $\mathbb{P}^l_{\mathrm{c}|\boldsymbol{r}} = \|e^{\boldsymbol{T}_k}\|_1$.

Important insights on the coverage probability can be obtained from (9). First, if the collaboration distance $R_c$ increases, both the probability $\mathbb{P}_\kappa$ and the integrand value in (9) increase, and, thus, the coverage probability grows accordingly. Furthermore, the effect of the BS density $\lambda_b$ on the coverage probability is two-fold. On the one hand, the average number of BSs increases with $\lambda_b$ as characterized by $\mathbb{P}_\kappa$, which results in a higher desired signal power. On the other hand, this advantage is counter-balanced by the increase in (LoS) interference power when $\lambda_b$ increases, as captured in the decaying exponential functions in (32). Additionally, this compact representation, i.e., $\mathbb{P}^l_{\mathrm{c}|\boldsymbol{r}} = \|e^{\boldsymbol{T}_K}\|_1$, leads to valuable system insights. For instance, the impact of the shape parameter $K = \kappa m_l$ on the intended channel gain $\mathrm{Gamma}(K, \theta)$ is rigorously captured by the finite sum representation in (30) of Appendix A, which is typically related to the collaboration distance $R_c$ and the Nakagami fading parameter $m_l$.

Next, we derive an LB on the coverage probability, which will lead to closed-form expressions for $t_k$, i.e., the entries populating $\boldsymbol{T}_K$ in (9). Given the high-altitude assumption of UAV-UEs, we will consider a special case when interfering BSs have dominant LoS communications to the typical UAV-UE, i.e, $\mathbb{P}_l(\upsilon) = 1$ and $\mathbb{P}_n(\upsilon) = 0$ in (9). Since this case results in higher interference power, this yields the derived coverage probability LB.

*Corollary 1: An LB on the coverage probability of the UAV-UEs can be computed from (9), where $\mathbb{P}^l_{\mathrm{c}|\boldsymbol{r}} = \|e^{\boldsymbol{T}_K}\|_1$, and the entries of $\boldsymbol{T}_K$ are given in closed-form expressions as*

$$t_k = \pi\lambda_b R_{ch}^2 \Big(\boldsymbol{1}\{k=0\} - c_{k2}F_1(k + m_l, k - \delta_l; k + 1 - \delta_l; -\varpi\varsigma R_{ch}^{-\alpha_l/2} m_l)\Big), \quad (10)$$

*where $c_k = \frac{\delta_l a_k \Gamma(k+m_l) m_l^{-k}}{(\delta_l - k)\Gamma(k+1)\Gamma(m_l)}$, $a_k = (\varpi\varsigma R_{ch}^{-\alpha_l/2})^k$, $\varsigma = P_t A_l G_s$, $\delta_l = \frac{2}{\alpha_l}$, $R_{ch}^2 = R_c^2 + h^2$, $\boldsymbol{1}\{.\}$ is the indicator function, and ${}_2F_1(\cdot,\cdot;\cdot;\cdot)$ is the ordinary hypergeometric function.*

*Proof:* Please see Appendix B. □

For comparison purposes, next, we derive the UAV-UE coverage probability under the nearest association scheme.

*Corollary 2: The coverage probability of the UAV-UEs under the nearest association scheme is:*

$$\mathbb{P}_{\mathrm{c}} = \int_0^{\infty} \mathbb{P}^l_{\mathrm{c}|r_0} f_{R_0}(r_0) \mathrm{d}r_0, \quad (11)$$

*where $\mathbb{P}^l_{\mathrm{c}|r_0} = \|e^{\boldsymbol{T}_{m_l}}\|_1$, $\boldsymbol{T}_{m_l}$ is defined as $\boldsymbol{T}_K$ in (9), with $\Omega(\varpi) = -2\pi\lambda_b \int_{\upsilon=r_0}^{\infty} \Big(1 - \delta_l \mathbb{P}_l(\upsilon) - \delta_n \mathbb{P}_n(\upsilon)\Big)\upsilon \mathrm{d}\upsilon$, $\varpi = \frac{\vartheta m_l}{P_t \zeta_l(r_0)}$, and $f_{R_0}(r_0) = 2\pi\lambda_b r_0\ e^{-\pi\lambda_b r_0^2}$ is the 2D serving distance PDF.*

*Proof:* The proof follows directly from [11] and Theorem 1, and hence is omitted for brevity. □

To verify the accuracy of our proposed approach, in Fig. 3, we show the theoretical UB and LB on the coverage probability of the UAV-UEs, and simulation of the UB based on (5). Fig. 3(a) shows that the Cauchy's inequality-based UB is remarkably tight. Moreover, although the obtained UB expression in (9) is less tight, it still represents a reasonably tractable bound on the exact coverage probability. Hence, (9) can be treated as a proxy of the exact result. Recall that (5) is based on an UB on a square of a sum of $\mathrm{Nakagami}$-$m_l$ RVs while the expression in (9) goes further by two more steps. First, we approximate the sum of Gamma RVs to an equivalent Gamma RV. Then, we round the shape parameter of the yielded Gamma RV to an integer $m_l\kappa$. Finally, the LB based on (10) can be also seen as a relatively looser bound than the UBs. As evident from Fig. 3, allowing CoMP transmission significantly enhances the coverage probability, e.g., from $28\%$ for the baseline scenario with nearest serving BSs to $60\%$ at $\vartheta = -5\mathrm{dB}$ (for an average of 2.5 cooperating BSs). In Fig. 3, the performance of UAV-UEs is also compared to that of their

[1] Although there exists an infinite sum in (9), this sum vanishes for a small number of serving BSs that is determined by the collaboration distance $R_c$ and the BSs' density $\lambda_b$.

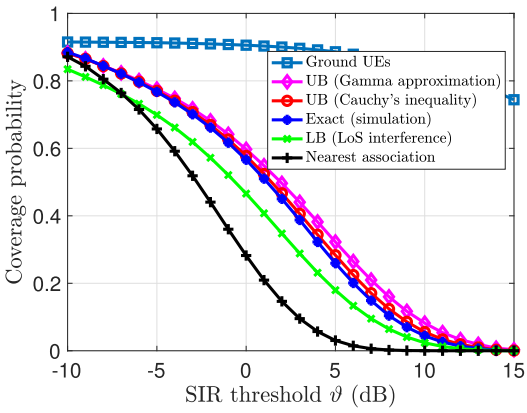


(a) Inter-cluster half distance $R_h = 190\,\mathrm{m}$

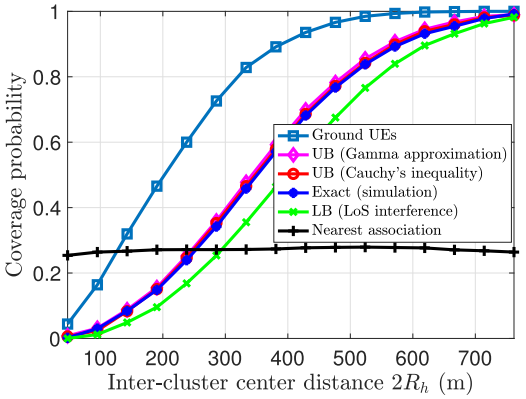


(b) SIR threshold $\vartheta = 0\,\mathrm{dB}$

Fig. 3. The derived upper and lower bounds on the coverage probability of UAV-UEs are plotted versus the SIR threshold $\vartheta$ and collaboration distance $R_c$: $\lambda_b = 20\ \mathrm{km}^{-2}$, $R_{\mathrm{sim}} = 20\ \mathrm{km}^2$, $\alpha_l = 2.09$, $\alpha_n = 3.75$, $h_{\mathrm{BS}} = 30$ m, $m_l = 3$, $A_l = 0.0088$, $A_n = 0.0226$, $h_d = 120$ m, $a = 0.3$, $b = 300\ \mathrm{km}^{-2}$, and $c = 20$ m.

ground counterparts experiencing Rayleigh fading and NLoS communications. We assume that the BSs' antennas are ideally down-tilted accounting for the ground UEs, i.e., the antenna gains for desired and interfering signals are $G_m$ and $G_s$, respectively. Under such a setup, we observe that the coverage probability of ground UEs substantially outperforms that of UAV-UEs, especially at high SIR thresholds. Fig. 3(b) shows the prominent effect of the collaboration distance $R_c$ on the coverage probability of ground and aerial UEs. We can see that for both kind of UEs, the coverage probability monotonically increases with $R_c$ since more BSs cooperate to serve the UEs when $R_c$ increases. Moreover, due to the down-tilt of the BSs' antennas and LoS-dominated interference for UAV-UEs, the coverage probability of ground UEs outperforms that of the UAV-UEs. However, we can see that the rate of coverage probability improvement with $R_c$, i.e., the slope, is higher for the UAV-UE. This can be interpreted by the fact that increasing $R_c$ yields more LoS signals within the desired signal side and subtracts them from the interference. Conversely, for ground UEs, the transmission is dominated by NLoS signals and Rayleigh fading.

Having characterized the performance of static UAV-UEs, next, we turn our attention to applications in which the UAV-UEs can be mobile. It is anticipated that mobile UAV-UEs will span a wide variety of applications, e.g., flying taxis and delivery drones. Hence, it is quite important to ensure reliable connections in the presence of UAV-UE mobility by potentially mitigating the LoS interference through CoMP transmissions. Moreover, unlike the ground UEs that can only move horizontally, UAV-UEs can fly in 3D space. Hence, a 3D mobility model is essential to convey a realistic description of the performance of mobile UAV-UEs. As a first step in this direction, we develop a novel 3D random waypoint (RWP) mobility model that effectively captures the vertical displacement of UAV-UEs, along with their typical 2D spatial mobility. The use of RWP mobility is motivated by its simplicity and tractability that is widely adopted in the mobility analysis in cellular networks [38]–[41]. Moreover, as we will discuss shortly, it has tunable parameters that can be set to appropriately describe the mobility of different mobile nodes, ranging from walking or driving users to 3D UAVs, [23] and [41].

## IV. 3D Mobility and Handover Analysis

Recently, the support of mobile drones such as UAV-UEs and UAV-BSs has been explored in 3GPP standardization efforts [31]. Particularly, there has been an increasing interest in the community to characterize the effect of the mobility of drones on their performance, whether they are cellular-connected UAVs or aerial BSs [22]–[28]. Motivated by this, we develop a novel stochastic 3D mobility model for multiple mobile UAV-UEs in random networks. Our proposed model provides a rich set of combinations to study various real-world UAV-UE deployment scenarios. Particularly, the proposed mobility framework could effectively model scenarios in which the information about the locations of UAVs exhibits randomness or uncertainty. For instance, in applications such as target scanning for reconnaissance, search and rescue, or random arrival of package delivery drones, the precise information about different strategic locations of multiple drones might be unavailable [23]. Moreover, in applications that rely on mobile, autonomous UAV-UEs in which drones intelligently update their locations based on the dynamics of their environments, the trajectories of the UAVs can neither be pre-planned nor fully deterministic [21]. This indeed resembles another scenario that is effectively characterized by stochastic mobility models.

Next, we illustrate the various elements of our proposed model. Then, we characterize the handover rate and handover probability for mobile UAV-UEs. Since we introduce the first study on 3D mobile UAV-UEs, for completeness, we consider two cases: UAV-UEs under CoMP transmissions, and UAV-UEs served by the nearest ground BS.

In the classical 2D mobility model, the spatial motion is considered only through a displacement and an angle. However, for the UAV-UE, due to the mission requirements, and environmental and atmospherical conditions, the UAV-UEs must change their altitude and make vertical motions. For instance, due to variations in the altitudes of buildings, UAV-UEs might have frequent up and down displacements along their trajectories. Indeed, the vertical motion is always

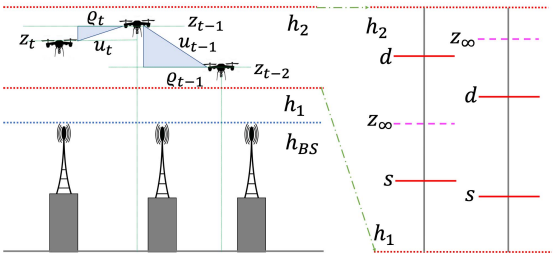


Fig. 4. A sample trace of the proposed 3D RWP mobility model, and an illustration of the 1D RWP vertical mobility of [23].

associated with the take-off and landing of UAV-UEs. This inherently triggers the concept of 3D mobility in 3D space.[2]

First, recall that in a classical RWP mobility model [38]–[41], the movement trace of a node (e.g., the UAV-UE) can be formally described by an infinite sequence of tuples: $\{(\boldsymbol{X}_{t-1}, \boldsymbol{X}_t, V_t)\}$, $\forall \boldsymbol{X}_t \in \mathbb{R}^3$, and $t \in \mathbb{N}$, where $t$ is the movement epoch and $\boldsymbol{X}_t = (\varrho_t, \phi_t, z_t)$ is the 3D cylindrical displacement of the UAV-UE at epoch $t$, see Fig. 4. During the $t$-th movement epoch, $\boldsymbol{X}_{t-1}$ denotes the starting waypoint, $\boldsymbol{X}_t$ denotes the target waypoint, and $V_t$ is the UAV-UE speed that follows a generalized PDF $f_{V_t}(\nu_t)$. Given the current waypoint $\boldsymbol{X}_{t-1}$, the next waypoint $\boldsymbol{X}_t$ is chosen such that the included angle $\phi_t$ between the projection of the vector $\boldsymbol{X}_{t-1} - \boldsymbol{X}_t$ on the $x$-$y$ plane and the abscissa is uniformly distributed on $[0, 2\pi]$. We define the transition length as the Euclidean distance between two 3D successive waypoints, i.e., $u_t = \|\boldsymbol{x}_t - \boldsymbol{x}_{t-1}\| = \sqrt{\varrho_t^2 + (z_t - z_{t-1})^2}$. Furthermore, the vertical displacement between two consecutive points, i.e., the change in $z$-axis, is also distributed according to a RV. We also let $\varphi_t$ be the acute angle of $u_t = \|\boldsymbol{x}_t - \boldsymbol{x}_{t-1}\|$ relative to the horizontal line $\rho_t$.

The selection of waypoints is assumed to be independent and identical for each movement epoch, and there is no pause time at these waypoints [39]. Particularly, similar to [41], the horizontal transition lengths $\{\rho_1, \rho_2, \dots\}$ are chosen to be i.i.d. with the cumulative distribution function (CDF) $F_{\rho_t}(\varrho_t) = 1 - \exp(-\pi\mu\varrho_t^2)$, i.e., the spatial transition lengths are Rayleigh distributed in $\mathbb{R}^2$ with mobility parameter $\mu$. The corresponding displacement PDF is hence $f_{\rho_t}(\varrho_t) = \frac{\partial F_{\rho_t}(\varrho_t)}{\partial \varrho_t} = 2\pi\mu\varrho_t e^{-\pi\mu\varrho_t^2}$. As also done in [23] and [22], we adopt a uniform distribution for the vertical displacement, however, the analysis for generalized PDFs can readily follow. In particular, we assume that $Z_t$ is uniformly distributed on $[h_1, h_2]$, i.e., $Z_t \sim \mathcal{U}(h_1, h_2)$ and $f_{Z_t}(z_t) = \frac{1}{h_2 - h_1}, \forall h_1 \leq z_t \leq h_2$. We henceforth refer to $\hbar = h_2 - h_1$ as altitude difference. Since the major restrictions of all drones' operations are their flying altitudes, it is reasonable to assume that $Z_t$ is bounded by $h_1$ and $h_2$. For instance, UAVs cannot fly higher than certain altitudes (above ground level (AGL)) that are typically chosen below the cruising altitude of manned aircrafts. The UAVs also have an inherent minimum altitude of zero AGL. However, due to mission requirements as well as environmental and atmospherical conditions, it is reasonable to assume $h_1 > 0$. We further assume that $h_1 > h_{\mathrm{BS}}$ for a high altitude UAV-UEs scenario. For simplicity, we assume that the UAV-UE moves with a constant speed $\bar{\nu}$. However, the analysis for generalized PDFs $f_{V_t}(\nu_t)$ of the speed can be done by using the same methodology. Finally, for the 3D displacement, we have $u_t = \sqrt{\varrho_t^2 + (z_t - z_{t-1})^2}$.

Under the proposed mobility model, several mobility patterns can be captured by choosing different mobility parameters and altitude thresholds. For example, larger values of $\mu$ statistically imply that the 2D and, consequently, 3D transition lengths are shorter. This means that the movement direction switch rates are higher. These values of the mobility parameter appropriately describe the motion of UAV-UEs frequently traveling between nearby hovering locations such as for the use case of aerial surveillance cameras. In contrast, a smaller $\mu$ statistically implies that the 2D and 3D transition lengths are longer and the corresponding movement direction switch rates are lower. These values of $\mu$ would be suitable to describe the motion of UAV-UEs traveling large distances such as for the use case of flying taxis and delivery drones. As a special case, if there is no change in the UAV-UE altitude along its trajectory, i.e., $h_1 = h_2 = h_d$, then the UAV-UE would move along straight lines in random directions with a constant speed, which is perhaps the simplest mobility model. This model is known to provide performance bounds and useful insights in wireless networks [25] and [42]. This model has also been recently adopted to model drone mobility in 3GPP studies related to drone networks [31]. In contrast, if the vertical mobility is solely considered, our model can efficiently describe the UAV-UE movements during take off and landing [43] and [44].

Given the independence assumption between $Z_t$ and $\rho_t$, we obtain their joint PDF from $f_{\rho_t, Z_t}(\varrho_t, z_t) = f_{\rho_t}(\varrho_t) f_{Z_t}(z_t) = \frac{2\pi\mu\varrho_t}{\hbar} e^{-\pi\mu\varrho_t^2}$, $\forall h_1 \leq z \leq h_2, 0 \leq \varrho \leq \infty$. Consequently, the PDF of the 3D displacement $f_{U_t}(u_t)$ is readily obtained in the next lemma.

*Lemma 1: The PDF of the 3D transition lengths $U_t$ is given by $f_{U_t}(u_t) = 2\pi\mu u_t e^{-\pi\mu u_t^2}\Omega(\mu, \hbar)$, where $\Omega(\mu, \hbar) = \frac{\pi\hbar\sqrt{\mu}\mathrm{erfi}\left(\sqrt{\pi\mu}\hbar\right) - e^{\pi\mu\hbar^2} + 1}{\pi\mu\hbar^2}$, and $\mathrm{erfi}(.) = \frac{-2i}{\sqrt{\pi}} \int_0^x e^{-t^2} dt$.*

*Proof:* We can reach this result by transforming the RVs $Z_t$, $Z_{t-1}$, and $\rho_t$ to $U_t$, where $u_t = \sqrt{\varrho_t^2 + (z_t - z_{t-1})^2}$, with the details omitted due to space limitations. □

*Remark 1:* If $h_1 = h_2$, it can be easily verified that $\lim_{\hbar \to 0} \Omega(\mu, \hbar) \to 1$, and $f_{U_t}(u_t) = 2\pi\mu u_t e^{-\pi\mu u_t^2}$. This shows that if the UAV-UE moves only along a horizontal plane, the PDF of the 3D displacement distance is reduced to its 2D counterpart, which verifies the correctness of the obtained 3D displacement distribution $f_{U_t}(u_t)$.

Having described the various elements of our proposed 3D RWP model, our immediate objective is to characterize the handover rate and handover probability for mobile UAV-UEs under CoMP transmissions and nearest association.

### *A. Handover Rate and Handover Probability for Nearest Association*

Assume that a mobile UAV-UE is located at $\boldsymbol{X}_{t-1}$ and let $\boldsymbol{X}_{t-1}$ and $\boldsymbol{X}_t$ be two arbitrary successive waypoints.

[2]We assume that the UAV-UEs are sparsely deployed such that there are no imposed constraints on the trajectories of different UAV-UEs. The analysis of multiple trajectories with such constraints is interesting but beyond the scope of this paper.

The handover rate is defined as the expected number of handovers per unit time. Hence, inspired from [41], we can compute the handover rate as follows. We first condition on an arbitrary position of the mobile UAV-UE $\boldsymbol{X}_t = \boldsymbol{x}_t$, and a given realization of the Poisson-Voronoi tessellation $\Phi_b$. Subsequently, the number of handovers will be equal to the number of intersections of the UAV-UE trajectory and the boundary of the Poisson-Voronoi tessellation. Then, by averaging over the spatial distribution of $\boldsymbol{X}_t$ and the distribution of Poisson-Voronoi tessellation, we derive the expected number of handovers. Alternatively, we notice that the number of handovers is equivalent to the number of intersections of the Poisson-Voronoi tessellation and the *horizontal projection of the segment* $\left[\boldsymbol{X}_{t-1}, \boldsymbol{X}_t\right]$ *on the* $x$-$y$ *plane*. Therefore, following [41], [45], [46], the expected number of handovers during one movement epoch will be: $\mathbb{E}\left[N\right] = \frac{2}{\pi}\sqrt{\frac{\lambda_b}{\mu}}$. The handover rate is then the ratio of the expected number of handovers during one movement $\mathbb{E}\left[N\right]$ to the mean time of one transition movement $\mathbb{E}\left[T\right]$. Since we have $\mathbb{E}[T] = \mathbb{E}[\frac{U_t}{V}] = \frac{\mathbb{E}[U_t]}{\bar{\nu}} = \frac{\Omega(\mu,\hbar)}{2\sqrt{\mu}\bar{\nu}}$, where $\mathbb{E}[U_t] = \frac{\Omega(\mu,\hbar)}{2\sqrt{\mu}}$, then, the handover rate will be:

$$H = \frac{\mathbb{E}[N]}{\mathbb{E}[T]} = \frac{2}{\pi}\sqrt{\frac{\lambda_b}{\mu}}\Bigg/\frac{\Omega(\mu,\hbar)}{2\sqrt{\mu}\bar{\nu}} = \frac{4\bar{\nu}\sqrt{\lambda_b}}{\pi\Omega(\mu,\hbar)}. \quad (12)$$

*Remark 2:* Unlike the handover rate for 2D RWP [41], [45], [46], $H$ in (12) is a function of the mobility parameter $\mu$ through $\Omega(\mu,\hbar)$. This captures the fact that, in the case of an UAV-UE, since each stochastically generated horizontal displacement is accompanied with a vertical one, the handover rate depends on $\mu$ that affects the vertical displacement switch rates.

Next, to characterize the coverage probability of mobile UAV-UEs, we use the concept of *handover probability*. Similar to [46] and [47], given the current location of a mobile UAV-UE, the handover probability is defined as the probability that there exists a BS closer than the serving BS after a unit time. From Fig. 5(a), for two arbitrary consecutive waypoints $\boldsymbol{X}_{t-1} = (\varrho_{t-1}, \phi_{t-1}, z_{t-1})$ and $\boldsymbol{X}_t = (\varrho_t, \phi_t, z_t)$, the horizontal speed of the UAV-UE from waypoint $\boldsymbol{X}_{t-1}$ to waypoint $\boldsymbol{X}_t$ is a RV whose realization is $V_h = \bar{\nu}\cos(\varphi_t)$, where $\varphi_t = \arccos\left(\frac{\varrho_t}{\sqrt{\varrho_t^2+(z_t-z_{t-1})^2}}\right)$. It is also assumed that the angle $\phi_t$ is taken with respect to the direction of connection as shown in Fig. 5(a). Define $\boldsymbol{q}_{t-1}$ and $\boldsymbol{q}_t$ in $\mathbb{R}^2$ as the horizontal projections of $\boldsymbol{X}_{t-1}$ and the location reached by the UAV-UE after a unit time, respectively. Fig. 5(a) illustrates that the UAV-UE is first associated with its nearest BS located at $\boldsymbol{q}_0$, i.e., there are no BSs in the ball of radius $r_0 = \|\boldsymbol{q}_{t-1} - \boldsymbol{q}_0\|$ centered at $\boldsymbol{q}_{t-1}$. Using the law of cosines, $\boldsymbol{q}_t$ is at distance $R = \sqrt{r_0^2 + (\bar{\nu}\cos(\varphi_t))^2 + 2r_0(\bar{\nu}\cos(\varphi_t))cos(\phi_t)}$ from the BS located at $\boldsymbol{q}_0$.[3]

The handover occurs only if another BS becomes closer to $\boldsymbol{q}_t$ than the serving BS located at $\boldsymbol{q}_0$, i.e., when there is at least one BS in the shaded area in Fig. 5(a). Therefore, given

[3]Since the UAV-UE starts from waypoint $\boldsymbol{X}_{t-1}$, we assume that it does not change its direction in a time shorter than the unit time. Hence, $q_t$ is assumed to be within the segment $[\boldsymbol{X}_{t-1}, \boldsymbol{X}_t]$ in Fig. 5.

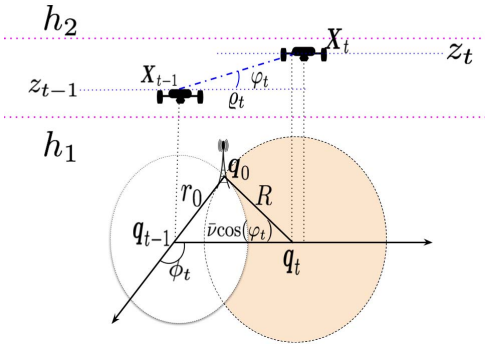


(a) Nearest association handover scenario

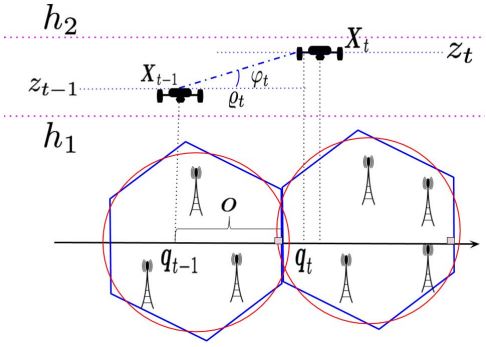


(b) Inter-CoMP handover scenario

Fig. 5. The probability of handover is computed based on the network geometry.

$\{r_0, z_{t-1}, z_t, \varrho_t, \phi_t\}$, the conditional probability of handover is $\mathbb{P}(H|r_0, z_{t-1}, z_t, \varrho_t, \phi_t)$

$$\begin{aligned} &= \mathbb{P}\Big(\mathcal{B}(\boldsymbol{q}_t, R) \setminus \mathcal{B}(\boldsymbol{q}_{t-1}, r_0) > 0 | r_0, z_{t-1}, z_t, \varrho_t, \phi_t\Big) \\ &\overset{(a)}{=} 1 - e^{-\lambda_b\left|\mathcal{B}(\boldsymbol{q}_t,R)\setminus\mathcal{B}(\boldsymbol{q}_{t-1},r_0)\right|} = 1 - e^{-\pi\lambda_b(R^2-r_0^2)} \\ &= 1 - e^{-\pi\lambda_b\left(r_0^2+(\bar{\nu}\cos(\varphi_t))^2+2r_0\bar{\nu}\cos(\varphi_t)cos(\phi_t)-r_0^2\right)}, \quad (13) \end{aligned}$$

where (a) follows from the void probability of PPP. $\mathcal{B}(\boldsymbol{q}_t, R)$ represents the ball with radius $R$ centered at $\boldsymbol{q}_t$ and $\mathcal{B}(\boldsymbol{q}_{t-1}, r_0)$ is excluded from $\mathcal{B}(\boldsymbol{q}_t, R)$ since the BS located at $\boldsymbol{q}_0$ is the nearest BS to $\boldsymbol{q}_{t-1}$. Finally, averaging over $Z_{t-1}, Z_t, \rho_t$, and $\phi_t$, where $\phi_t \sim \mathcal{U}(0, 2\pi)$, we get $\mathbb{P}(H|r_0)$

$$= 1 - \mathbb{E}_{\rho_t, Z_t, Z_{t-1}, \phi_t}\Big[e^{-\pi\lambda_b\left((\bar{\nu}\cos(\varphi_t))^2+2r_0(\bar{\nu}\cos(\varphi_t))cos(\phi_t)\right)}\Big]. \quad (14)$$

For the special case in which the UAV-UE moves radially away from the serving BS, i.e., $\phi_t = 0$, next, we obtain a tractable yet accurate UB on the conditional handover probability. This assumption is reasonable, particularly, if the UAV-UE follows a horizontally-direct path subject only to vertical fluctuations due to mission, environmental, and atmospherical conditions.

*Lemma 2: An UB on the conditional probability of handover is given by*

$$\mathbb{P}(H|r_0) = 1 - e^{-\frac{2\lambda_b r_0 \bar{\nu}}{\sqrt{\pi}\mu\hbar^2}\psi(\mu,\hbar)}e^{-\pi\lambda_b\zeta(\mu,\hbar)}, \quad (15)$$

*where* $\psi(\mu,\hbar) = \pi\hbar^2\mu G_{2,3}^{2,2}\Big(\hbar^2\pi\mu\Big|\begin{matrix}\frac{1}{2},\frac{1}{2}\\0,1,-\frac{1}{2}\end{matrix}\Big) - G_{2,3}^{2,2}\Big(\hbar^2\pi\mu\Big|\begin{matrix}1,\frac{3}{2}\\1,2,0\end{matrix}\Big)$, $G_{p,q}^{m,n}$ *denotes the Meijer G function, defined as*

$$G_{p,q}^{m,n}\Big(x\Big|\begin{matrix}a_1,\ldots,a_p\\b_1,\ldots,b_q\end{matrix}\Big) = \frac{1}{2\pi i}\int \frac{\prod_{j=1}^{m}\Gamma(b_j+s)\prod_{j=1}^{n}\Gamma(1-a_j+s)}{\prod_{j=n+1}^{p}\Gamma(a_j+s)\prod_{j=m+1}^{q}\Gamma(1-b_j+s)}x^s \mathrm{d}s, \tag{16}$$

*and* $\zeta(\mu,\hbar) = \bar{\nu}^2\big(1-\frac{2\pi\mu}{\hbar^2}\int_0^{\hbar}(\hbar-p)p^2\ e^{\pi\mu p^2}\Gamma\left(0,\pi p^2\mu\right)\mathrm{d}p\big)$.

*Proof:* Please see Appendix C. □

From (15), it is intuitive to see that $\mathbb{P}(H|r_0)$ increases with $\bar{\nu}$ and $\lambda_b$ because there will be a higher probability of handover when the UAV-UE speed is higher, and the network is denser. Moreover, $\mathbb{P}(H|r_0)$ decreases as the term $\mu\hbar^2$ increases. This reveals important insights on the effect of the altitude difference $\hbar$ and the density $\mu$. Particularly, the handover probability decreases when the UAV-UE jointly has higher direction switch rates (higher $\mu$) and larger altitude difference $\hbar$. Next, we obtain the handover rate for UAV-UEs under CoMP transmissions.

### *B. Inter-CoMP Handover Rate and Handover Probability*

We define the number of handovers $\mathbb{E}[N]$ as the number of intersections of the horizontal projection of the segment $\left[\boldsymbol{X}_{t-1},\boldsymbol{X}_t\right]$ and the boundaries of disjoint clusters whose inter-cluster center distance is $2R_h$, as discussed in Section II. The hexagonal cell has six sides of length $\ell = \frac{2R_h}{\sqrt{3}}$. Following the Buffon's needle approach for hexagonal cells [46], we next obtain the inter-CoMP handover rate.

*Proposition 1: The inter-CoMP handover rate for a network of disjoint clusters whose inter-cluster center distance is* $2R_h$ *is given by*

$$H = \frac{\mathbb{E}[N]}{\mathbb{E}[T]} \tag{17}$$

$$= 2\frac{\pi\hbar^2\mu G_{2,3}^{2,2}\Big(\hbar^2\pi\mu\Big|\begin{matrix}\frac{1}{2},\frac{1}{2}\\0,1,-\frac{1}{2}\end{matrix}\Big) - G_{2,3}^{2,2}\Big(\hbar^2\pi\mu\Big|\begin{matrix}1,\frac{3}{2}\\1,2,0\end{matrix}\Big)}{\pi\sqrt{\pi}R_h\hbar^2\mu}\bar{\nu}. \tag{18}$$

*Proof:* Please see Appendix D. □

We now characterize the UAV-UE inter-CoMP handover probability. To keep the analysis simple, we consider a special case in which the UAV-UE moves perpendicularly to the inter-cluster boundaries, as shown in Fig. 5(b). As discussed in Section IV-A, this is a practical assumption for a UAV-UE that follows a horizontally straight path subject only to vertical fluctuations. Moreover, since these boundaries represent virtual borders between disjoint clusters, the assumption that such boundaries are in a direction perpendicular to the UAV-UE trajectory is quite reasonable. Hence, the UAV-UE moves by a horizontal distance $\bar{\nu}\cos(\varphi_t)$ in a unit of time in a direction perpendicular to the inter-cluster boundaries. A handover occurs if the horizontal distance traveled is larger than the distance $o$ to the cluster side, which is a realization of RV $O$ whose PDF is $f_O(o)$. Conditioning on $O=o$, the handover probability is formally stated as $\mathbb{P}(H|o)$

$$= \mathbb{P}\big(\frac{\bar{\nu}\varrho_t}{\sqrt{\varrho_t^2+(z_t-z_{t-1})^2}} > o\big) = \mathbb{P}\big(\varrho_t > \frac{o(z_t-z_{t-1})}{\sqrt{\bar{\nu}^2-o^2}}\big)$$

$$= \mathbb{E}_{Z_t,Z_{t-1}}\int_{\varrho_t=\frac{o(z_t-z_{t-1})}{\sqrt{\bar{\nu}^2-o^2}}}^{\infty} 2\pi\mu\varrho_t e^{-\pi\mu\varrho_t^2}\mathrm{d}\varrho_t \tag{19}$$

$$\overset{(a)}{=} \mathbb{E}_{Z_t,Z_{t-1}} e^{-\pi\mu\left(\frac{o^2(z_t-z_{t-1})^2}{\bar{\nu}^2-o^2}\right)} \overset{(b)}{=} \mathbb{E}_p e^{-\pi\mu p^2\frac{o^2}{\bar{\nu}^2-o^2}}$$

$$\overset{(c)}{=} \frac{1}{\hbar^2}\frac{\hbar\sqrt{\frac{\mu o^2}{\bar{\nu}^2-o^2}}\mathrm{erf}\left(\sqrt{\pi}\hbar\sqrt{\frac{o^2}{\bar{\nu}^2-o^2}}\sqrt{\mu}\right) + \frac{e^{-\pi\mu\hbar^2\frac{o^2}{\bar{\nu}^2-o^2}}-1}{\pi}}{\frac{\mu o^2}{\bar{\nu}^2-o^2}} \tag{20}$$

$$= \frac{1}{\hbar}\frac{\mathrm{erf}\left(\sqrt{\pi}\hbar\sqrt{\frac{\mu o^2}{\bar{\nu}^2-o^2}}\right)}{\sqrt{\frac{\mu o^2}{\bar{\nu}^2-o^2}}} + \frac{1}{\pi\hbar^2}\frac{e^{-\pi\mu\hbar^2\frac{o^2}{\bar{\nu}^2-o^2}}-1}{\frac{\mu o^2}{\bar{\nu}^2-o^2}}, \tag{21}$$

where (a) follows from solving the integral of (19), (b) follows from change of variables $p = z_t - z_{t-1}$, with $f_P(p) = \frac{\hbar-|p|}{\hbar^2}, -\hbar \le p \le \hbar$, and (c) follows from taking the expectation with respect to (w.r.t.) $p$. Note that $O$ is a uniform RV in $[0, 2R_h]$ that models the distance between the UAV-UE and the inter-cluster boundaries, see Fig. 3(b). Averaging over $O$ given that $f_O(o) = \frac{1}{2R_h}, 0 < o < 2R_h$, we get $\mathbb{P}(H)$. However, we observe that if $o > \bar{\nu}$, the handover probability will be zero since the UAV-UE can not travel the distance $o$ in a unit of time, hence, we have

$$\mathbb{P}(H) = \frac{1}{2R_h\hbar}\int_{o=0}^{\bar{\nu}}\frac{\mathrm{erf}\left(\sqrt{\pi}\hbar\sqrt{\frac{\mu o^2}{\bar{\nu}^2-o^2}}\right)}{\sqrt{\frac{\mu o^2}{\bar{\nu}^2-o^2}}} + \frac{1}{2\pi R_h\hbar^2}\int_{o=0}^{\bar{\nu}}\frac{e^{-\pi\mu\hbar^2\frac{o^2}{\bar{\nu}^2-o^2}}-1}{\frac{\mu o^2}{\bar{\nu}^2-o^2}}. \tag{22}$$

Fig. 6 verifies the accuracy of the obtained handover probabilities. Fig. 6(a) presents the handover probability versus BSs' intensity $\lambda_b$ under the nearest association scheme. The figure shows that the obtained UB in (15) is quite tight. It is also noted that as long as the UAV-UE has frequent vertical movements, i.e., larger $\hbar$, the handover probability is lower since the effective horizontal travelled distance becomes shorter. The handover probability also monotonically increases with $\lambda_b$ since a higher rate of handover occurs for denser networks. Fig. 6(b) shows the inter-CoMP handover probability versus the inter-cluster center distance $2R_h$. The handover probability monotonically decreases with $R_h$ since a lower rate of handover is anticipated when the cluster size increases. Next, we will use our proposed RWP model to obtain the coverage probability of 3D mobile UAV-UEs.

## V. Coverage Probability of Mobile UAV-UEs

Next, we will employ the handover probabilities in (15) and (22) to quantify the coverage probability of mobile UAV-UEs under the nearest association and CoMP transmissions, respectively. It is worth highlighting that (9) represents the probability that a static UAV-UE is in coverage with

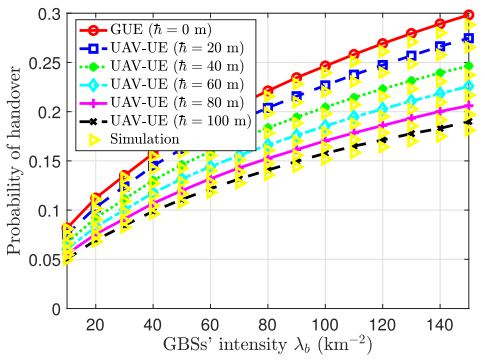


(a) Nearest association scenario

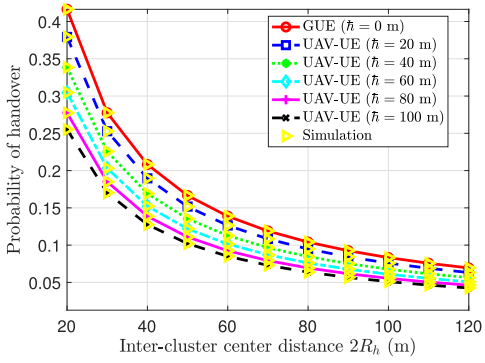


(b) CoMP transmission scenario

Fig. 6. The probability of handover is plotted versus network parameters for nearest association and CoMP transmission schemes ($\bar{\nu} = 30$ kmh, $\mu = 300$ km$^{-2}$, $h_1 = 100$ m).

neither mobility nor handover considered. However, mobile UAV-UEs are susceptible to frequent handovers that would negatively impact their performance. For instance, handover typically results in dropped connections and causes longer service delays. In fact, higher handover rates lead to a higher risk of quality-of-service (QoS) degradation.

To account for the user mobility, similar to [46]–[48], we consider a linear function that reflects the cost of handovers. Under this model, the UAV-UE coverage probability can be defined as:

$$P_c(\bar{\nu}, \mu, \beta) = \mathbb{P}(\Upsilon \geq \vartheta, \bar{H}) + (1-\beta)\mathbb{P}(\Upsilon \geq \vartheta, H), \quad (23)$$

where the first term represents the probability that the UAV-UE is in coverage and no handover occurring. Besides, the second term is the probability that the UAV-UE is in coverage and handover occurs penalized by a handover cost, where $\beta \in [0,1]$ represents the probability of connection failure due to handover. The coefficient $\beta$, in effect, measures the system sensitivity to handovers, which highly depends on the hysteresis margin and ping-pong rate [45]–[48]. Our goal is to obtain the coverage probability of a mobile UAV-UE for a given handover penalty $\beta$ [46]. After some manipulations, we can rewrite (23) as

$$P_c(\bar{\nu}, \mu, \beta) = (1-\beta)\mathbb{P}(\Upsilon \geq \vartheta | r_0) + \beta\mathbb{P}(\Upsilon \geq \vartheta, \bar{H} | r_0). \quad (24)$$

To obtain $P_c(\bar{\nu}, \mu, \beta)$, we first need to calculate the statistical distribution of the UAV-UE altitude for our proposed 3D mobility model. As shown in Fig. 4, the 3D mobility model defines the vertical movement of the UAV-UE in a finite region $[h_1, h_2]$, *referred to as vertical 1D RWP* as in [23]. Initially, at time instant $t_0$, the UAV-UE is at an arbitrary altitude $h_0$ selected uniformly from the interval $[h_1, h_2]$. Then, at next time epoch $t_1$, this UAV-UE at $h_0$ selects a new random waypoint $h_1$ uniformly in $[h_1, h_2]$, and moves towards it (along with the spatial movement characterized by $f_{\rho_t}(\varrho_t)$). Once the UAV-UE reaches $h_1$, it repeats the same procedure to find the next destination altitude and so on. After a long running time, the steady-state altitude distribution converges to a *nonuniform distribution* $F_{Z_\infty}(z_\infty)$ [38], where $Z_\infty$ is a RV representing the steady state vertical location of the UAV-UE. Note that random waypoints refer to the altitude of a UAV-UE at each time epoch, which is uniformly-distributed in $[h_1, h_2]$, while vertical transitions are the differences in the UAV-UE altitude throughout its trajectory. While the random waypoints are independent and uniformly distributed by definition, the random lengths of vertical transitions are not statistically independent. This is because the endpoint of one movement epoch is the starting point of the next epoch. In [38], it is shown that $F_{Z_\infty}(z_\infty) = \frac{\mathbb{E}[L_{z_\infty}]}{\mathbb{E}[L]}$, where $L_{z_\infty}$ and $L$ denote the length $\|z_\infty - h_1\|$, and the entire movement length at any given epoch, respectively. From [38], we have $\mathbb{E}[L] = \frac{\hbar}{3}$ and $\mathbb{E}[L_{z_\infty}]$ can be similarly derived from:

$$\mathbb{E}[L_{z_\infty}] = \int_{s=h_1}^{h_2}\int_{d=h_1}^{h_2} l_{z_\infty}(s,d) f_S(s) f_D(d) \mathrm{d}d\mathrm{d}s, \quad (25)$$

where $s$ and $d$ refer to the source and destination of a movement, respectively; $f_S(s) = f_D(d) = \frac{1}{\hbar}$, $h_1 \leq s, d \leq h_2$, see the right side of Fig. 4. $l_{z_\infty}(s,d)$ denotes the value of the random variable $L_{z_\infty}$ if $S = s$ and $D = d$. Because of the symmetry of $s$ and $d$, it is sufficient to restrict the calculation to epochs with $s < d$, and then multiply the result by a factor of two. A necessary condition for $l_{z_\infty}(s,d) \neq 0$ is that $s \leq z_\infty$. From Fig. 4, if $d \leq z_\infty$, we have $l_{z_\infty}(s,d) = d - s$, however, if $d > z_\infty$, we get $l_{z_\infty}(s,d) = z_\infty - s$, which yields

$$\begin{aligned}
&\mathbb{E}[L_{z_\infty}] \\
&= \frac{2}{\hbar^2}\int_{s=h_1}^{z_\infty}\int_{d=s}^{z_\infty}(d-s)\mathrm{d}d\mathrm{d}s \\
&\quad + \frac{2}{\hbar^2}\int_{s=h_1}^{z_\infty}\int_{d=z_\infty}^{h_2}(z_\infty - s)\mathrm{d}d\mathrm{d}s \\
&= \frac{2}{\hbar^2}\Big(-\frac{h_1^3}{6} + \frac{h_1^2 h_2}{2} - h_1 h_2 z_\infty + \frac{h_1 z_\infty^2}{2} + \frac{h_2 z_\infty^2}{2} - \frac{z_\infty^3}{3}\Big).
\end{aligned} \quad (26)$$

Therefore, the PDF of $Z_\infty$ is given by

$$\begin{aligned}
f_{Z_\infty}(z_\infty) &= \frac{\partial F_{Z_\infty}(z_\infty)}{\partial z_\infty} = \frac{\partial}{\partial z_\infty}\frac{\mathbb{E}[L_{z_\infty}]}{\mathbb{E}[L]} \\
&= \frac{h_1 z_\infty + h_2 z_\infty - h_1 h_2 - z_\infty^2}{\hbar^3/6} \quad \forall h_1 < z_\infty < h_2,
\end{aligned} \quad (27)$$

and the corresponding mean is given by $\mathbb{E}[Z_\infty] = \frac{1}{2\hbar^3}\big(h_2^4 - h_1^4 + 2h_1^3\ h_2 - 2h_1\ h_2^3\big)$. Next, we will use the derived PDF $f_{Z_\infty}(z_\infty)$, along with the probability of handover from the

previous section, to fully characterize $P_c(\bar{\nu},\mu,\beta)$ under the nearest association and CoMP transmissions.

### A. Coverage Probability for Nearest Association

Next, we derive the coverage probability of a mobile UAV-UE under the nearest association scheme. Observing (24), for a given $\beta$, we must compute $\mathbb{P}(\Upsilon \geq \vartheta, \bar{H}|r_0)$ to obtain $P_c(\bar{\nu},\mu,\beta)$. The former probability is basically the joint event of being in coverage and no handover occurs. We adopt the tight UB on the handover probability obtained in (15), where $\mathbb{P}(\bar{H},r_0) = 1-\mathbb{P}(H,r_0)$ is the conditional probability of no handover. Unlike static UAV-UEs, under the 3D RWP model, both the altitude of the UAV-UE and the horizontal distance $R_0$ to the nearest BS are RVs. Since $R_0$ and $Z_\infty$ are two independent RVs, we have $f_{R_0,Z_\infty}(r_0,z_\infty) = f_{R_0}(r_0)f_{Z_\infty}(z_\infty)$.

We assume that the UAV-UE has an arbitrary long trajectory that passes through nearly all SIR states. Therefore, the average SIR through a randomly selected UAV-UE trajectory is inferred from a stationary PPP analysis. This assumption, which is adopted in [46]–[48] for ground UEs, is practically reasonable for mobile UAV-UEs such as flying taxis and delivery drones that typically have sufficiently long trajectories. Given the handover probability in (15) and the linear function in (24), the coverage probability under the nearest association scheme is given below.

*Theorem 2: The coverage probability of a 3D mobile UAV-UE associated with its nearest BS is*

$$\begin{aligned} P_c(\bar{\nu},\mu,\beta) &= 2(1-\beta)\pi\lambda_b \times \int_{h_1}^{h_2}\int_0^\infty r_0 e^{-\pi\lambda_b r_0^2}\mathbb{P}^l_{\mathrm{c}|r_0,z_\infty} \\ &\times f_{Z_\infty}(z_\infty)\mathrm{d}r_0\mathrm{d}z_\infty + 2\beta\pi\lambda_b e^{-\pi\lambda_b\zeta(\mu,\hbar)} \\ &\times \int_{h_1}^{h_2}\int_0^\infty r_0 e^{-\pi\lambda_b r_0^2} e^{-\frac{2\lambda_b r_0\bar{\nu}}{\sqrt{\pi}\mu\hbar^2}\psi(\mu,\hbar)}\mathbb{P}^l_{\mathrm{c}|r_0,z_\infty} f_{Z_\infty}(z_\infty)\mathrm{d}r_0\mathrm{d}z_\infty, \end{aligned} \tag{28}$$

*where* $\mathbb{P}^l_{\mathrm{c}|r_0,z_\infty} = \|e^{\boldsymbol{T}_{m_l}}\|_1$, $\boldsymbol{T}_{m_l}$ *is defined as* $\boldsymbol{T}_K$ *in (9), with* $\Omega(\varpi)_{|r_0,z_\infty} = -2\pi\lambda_b\int_{\upsilon=r_0}^\infty \big(1-\delta_l\mathbb{P}_l(\upsilon)-\delta_n\mathbb{P}_n(\upsilon)\big)\upsilon\mathrm{d}\upsilon$, $\delta_l = \Big(1+\frac{\varpi P_t A_l G_s(\upsilon^2+z_\infty^2)^{-\alpha_l/2}}{m_l}\Big)^{-m_l}$, $\delta_n = \Big(1+\frac{\varpi P_t A_n G_s(\upsilon^2+z_\infty^2)^{-\alpha_n/2}}{m_n}\Big)^{-m_n}$, *and* $\varpi = \frac{\vartheta m_l}{P_t A_l G_s(r_0^2+z_\infty^2)^{-\alpha_l/2}}$; $\psi(\mu,\hbar)$ *and* $\zeta(\mu,\hbar)$ *are given in Lemma 2.*

*Proof:* The first term in (28) is obtained directly from (24) and Corollary 2, where the UAV-UE altitude $h_d$ is replaced with the RV $z_\infty$ whose PDF is given in (27). Additionally, the second term in (28) represents the joint event of no handover and being in coverage, which is computed based on $\mathbb{P}(H|r_0,\phi)$ in (15). □

It is clear from (28) that, if $\beta = 1$, the first term vanishes and the UAV-UE will be in coverage only if there is no handover associated with its mobility. This is because the handover will always cause connection failure. Moreover, since it is hard to directly obtain insights from (28) on the effect of the altitude $z_\infty$ and the altitude difference $\hbar$, several numerical results based on (28) will be shown in Section VI to provide key practical insights. Next, we similarly derive the coverage probability of a mobile UAV-UE under CoMP transmission.

### B. Coverage Probability for CoMP Transmission

Similar to Section V-A, we employ the handover probability in (22) and the linear function in (24) to obtain the coverage probability under CoMP transmission. The probability of inter-cluster handover $\mathbb{P}(H)$ is derived in (22) assuming that the UAV-UE moves perpendicular to the cluster boundaries. To compute $\mathbb{P}(\Upsilon \geq \vartheta, \bar{H})$ in (24), the joint PDF of the serving distances needs to be characterized given the random location of the UAV-UE along its trajectory. However, for tractability, we consider the joint serving distances when the UAV-UE horizontal projection is at the cluster center. Therefore, the obtained performance can be seen as an UB on the performance of a randomly located UAV-UE. This assumption is in line with prior work [33] and the analysis for static UAV-UEs, where we sought an UB on the coverage probability.

Since $\boldsymbol{R}_\kappa = [R_1,\ldots,R_\kappa]$ and $Z_\infty$ are independent RVs, their joint PDF is $f_{\boldsymbol{R}_\kappa,Z_\infty}(\boldsymbol{r}_\kappa,z_\infty) = f_{\boldsymbol{R}_\kappa}(\boldsymbol{r}_\kappa)f_{Z_\infty}(z_\infty)$. Given (22) and (24), an UB on the coverage probability of a mobile UAV-UE under CoMP transmissions is obtained in the next theorem.

*Theorem 3: An UB on the coverage probability of a 3D mobile UAV-UE cooperatively served via CoMP transmission from BSs within a collaboration distance $R_c$ is given by:*

$$\begin{aligned} \mathbb{P}_{\mathrm{c}} = \big(1-\beta+\beta\times\mathbb{P}(\bar{H})\big)\sum_{\kappa=1}^\infty \mathbb{P}_\kappa \int_{h_1}^{h_2}\int_{\boldsymbol{r}_\kappa=\boldsymbol{R}_c}^\infty \mathbb{P}^l_{\mathrm{c}|\boldsymbol{r}_\kappa,z_\infty} \\ \times f_{Z_\infty}(z_\infty)\prod_{i=0}^{\kappa}\frac{2r_i}{R_c^2}\mathrm{d}\boldsymbol{r}_\kappa\mathrm{d}z_\infty, \end{aligned} \tag{29}$$

*where* $\mathbb{P}(\bar{H}) = 1-\mathbb{P}(H)$ *from (22),* $\mathbb{P}^l_{\mathrm{c}|\boldsymbol{r}_\kappa,z_\infty} = \|e^{\boldsymbol{T}_K}\|_1$, *and* $\boldsymbol{T}_K$ *is as defined in (9), with* $\Omega(\varpi)_{|\boldsymbol{r}_\kappa,z_\infty} = -2\pi\lambda_b\int_{\upsilon=R_c}^\infty \Big(1-\delta_l\mathbb{P}_l(\upsilon)-\delta_n\mathbb{P}_n(\upsilon)\Big)\upsilon\mathrm{d}\upsilon$, $\delta_l = \Big(1+\frac{\varpi P_t A_l G_s(\upsilon^2+z_\infty^2)^{-\alpha_l/2}}{m_l}\Big)^{-m_l}$, $\delta_n = \Big(1+\frac{\varpi P_t A_n G_s(\upsilon^2+z_\infty^2)^{-\alpha_n/2}}{m_n}\Big)^{-m_n}$, $\varpi = \frac{\vartheta}{\kappa P_t\theta}$, $\theta = \frac{\sum_i^\kappa \zeta_l(r_i)^2}{m_l\sum_i^\kappa\zeta_l(r_i)}$, *and* $\zeta_l(r_i) = A_l G_s\big(r_i^2+z_\infty^2\big)^{-\alpha_l/2}$.

*Proof:* The proof follows from (24) and Theorem 1, and is analogous to Theorem 2. □

The effect of $\beta$ on the coverage probability in (29) can be interpreted in a similar way to the nearest association scheme in (28). Moreover, conditioning on $Z_\infty = z_\infty$, and for a given $\beta$ in (29), the yielded expression holds the same insights as for static UAV-UEs in Section III-B. In particular, what the Nakagami fading parameter $m_l$, antenna down-tilting angle, and the collaboration distance $R_c$ entail for the performance of mobile UAV-UEs is similar to the that of static UAV-UEs. Finally, a simple lower bound on the mobile UAV-UE coverage probability can be obtained similar to Corollary 1, with the detailed omitted due to space limitation.

## VI. Simulation Results and Analysis

For our simulations, we consider a network having the parameter values indicated in Table II. In Fig. 7, we show

TABLE II
SIMULATION PARAMETERS

| Description | Parameter | Value |
|---|---|---|
| LoS path-loss exponent | $\alpha_l$ | 2.09 |
| NLoS path-loss exponent | $\alpha_n$ | 3.75 |
| LoS path-loss constant | $A_l$ | $-41.1$ dB |
| NLoS path-loss constant | $A_n$ | $-32.9$ dB |
| Nakagami fading parameter (LoS) | $m_l$ | 3 |
| Nakagami fading factor (NLoS) | $m_n$ | 1 |
| Area fraction occupied by buildings | $a$ | 0.3 |
| Density of buildings | $\eta$ | $300\,\text{km}^{-2}$ |
| Buildings height Rayleigh parameter | $c$ | 20 m |
| SIR threshold | $\vartheta$ | 0 dB |
| BSs' intensity | $\lambda_b$ | 20 BSs/km$^2$ |
| Inter-cluster center distance | $2R_h$ | 380 m |
| Antenna main-lobe gain | $G_m$ | 10 dB |
| Antenna side-lobe gain | $G_s$ | $-3.01$ dB |
| BS antenna height | $h_{\text{BS}}$ | 30 m |
| UAV-UE altitude | $h_d$ | 120 m |
| Simulation area | $R_{\text{sim}}$ | 20 km$^2$ |
| Mean altitude of mobile UAV-UEs | $\mathbb{E}[Z_\infty]$ | 150 m |

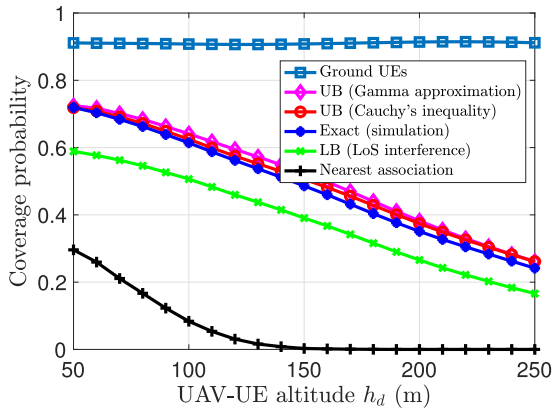


(a) UAV-UE coverage probability versus its altitude $h_d$

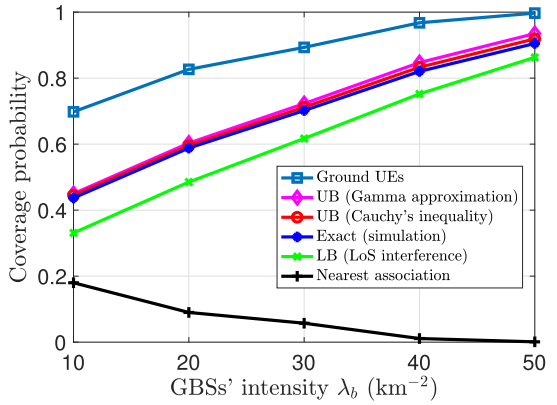


(b) UAV-UE coverage probability versus BS's intensity $\lambda_b$

Fig. 7. The derived upper and lower bounds on the static UAV-UE coverage probability are plotted versus the UAV-UE altitude $h_d$ and BSs' intensity $\lambda_b$.

the effect of the UAV-UE altitude and BSs' intensity on the coverage probability of static UAV-UEs, with that of ground UEs plotted for comparison. Fig. 7(a) shows that the coverage probability of high-altitude UAV-UEs monotonically decreases as $h_d$ increases. This is because, as the altitude of UAV-UEs increases, the received interference power substantially increases due to the dominance of LoS links. Fig. 7(a) also shows that the derived UB on the coverage probability in (9) is considerably tight. Meanwhile, Fig. 7(b) illustrates the effect of BSs' intensity $\lambda_b$ on the performance of UAV-UEs. Except for the nearest association scheme, the coverage probability improves with $\lambda_b$ since more BSs cooperate to serve the aerial (and ground) UEs. However, when the UAV-UE associates to its nearest BS, the effect of interference increases as the network becomes denser.

Next, we study the impact of 3D mobility on the performance of UAV-UEs. We further compare the performance of UAV-UEs with their ground counterparts moving horizontally with the same speed $\bar{\nu}$. In Fig. 8, the handover rate and coverage probability of mobile aerial and ground UEs associated with their nearest BSs are investigated. Fig. 8(a) plots the handover rate versus $\lambda_b$ at different values of the altitude difference $\hbar$. Fig. 8(a) shows that the analytical result in (12) matches the simulation result quite well. As is the case for typical Poisson-Voronoi models, the handover rate grows linearly with the square root of the BS's intensity $\sqrt{\lambda_b}$. Moreover, the handover rate decreases as $\hbar$ increases, which implies that a UAV-UE having frequent up and down motions along its trajectory is susceptible to lower rates of handover. We also note that the handover rate of UAV-UEs is upper bounded by that of ground UEs with $\hbar = 0$. Fig. 8(b) shows the effect of the UAV-UE speed $\bar{\nu}$ on its handover rate.[4] Intuitively, the handover rate increases as $\bar{\nu}$ increases since the UAV-UE stays shorter time in the area covered by each BS, i.e., shorter sojourn time. Finally, Fig. 8(c) investigates the effect of mobility on the UAV-UE coverage probability given an arbitrary handover penalty $\beta$. Notice that the coverage probability decreases as $\bar{\nu}$ increases since this leads to higher handover probability (penalized by $\beta$). Moreover, the altitude difference $\hbar$ has a marginal effect on the coverage probability of UAV-UEs. This is attributed to the fact that the increase of the altitude difference $\hbar$ for mobile UAV-UEs while keeping the same average flying altitude $\mathbb{E}[Z_\infty]$ relatively yields the same average coverage probability.

In Fig. 9, we evaluate the effect of the 3D mobility on the UAV-UE performance under CoMP transmissions. Fig. 9(a) shows that the inter-CoMP handover rate monotonically decreases as $R_c$ increases since the UAV-UE would have a longer sojourn time in each cluster. Moreover, the handover rate is shown to decrease as $\hbar$ increases, i.e., when the UAV-UE has frequent up and down motions along its trajectory. We also note that the handover rate of UAV-UEs is upper bounded by that of ground UEs, with $\hbar = 0$. Fig. 9(b) shows the effect of the UAV-UE speed $\bar{\nu}$ on the inter-CoMP handover. We note that this handover rate also increases as $\bar{\nu}$ increases since the UAV-UE will have a shorter sojourn time in each cluster. Finally, Fig. 9(c) shows the effects of the UAV-UE speed and altitude difference on the UAV-UE coverage probability. Fig. 9(c) shows that the UB on the coverage probability, characterized in Theorem 3, slightly decreases

[4]Low values of the speed $\bar{\nu}$ suits the motion of UAV-UEs such as surveillance cameras while higher velocities would be suitable for UAV-UEs such as flying taxis.

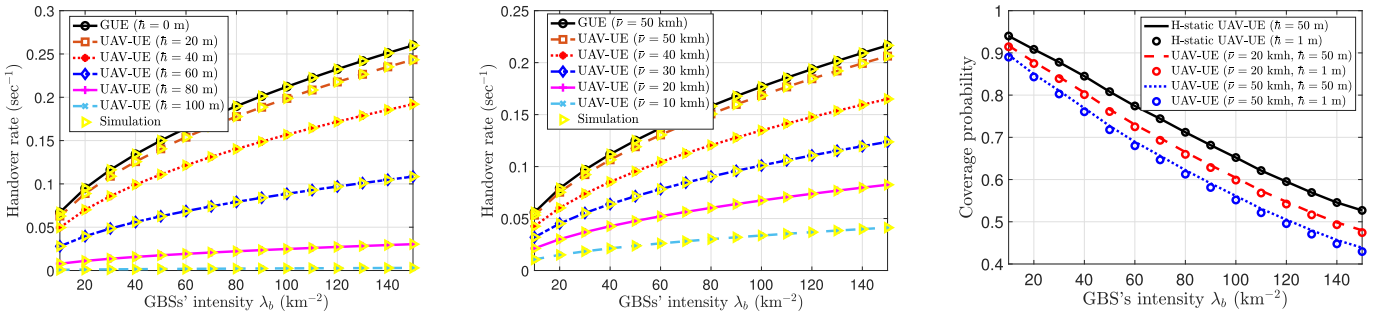


(a) $\bar{\nu} = 50\,\text{kmh}$, $\mu = 300\,\text{km}^{-2}$ (b) $\hbar = 30\,\text{m}$, $\mu = 300\,\text{km}^{-2}$ (c) $\beta = 0.5$, $\mu = 100\,\text{km}^{-2}$, $\vartheta = -10\,\text{dB}$

Fig. 8. Effect of the 3D mobility on the performance of aerial and UEs when they are associated with their nearest BSs. In (c), H-static refers to a UAV-UE that only moves in the vertical direction within an altitude difference $\hbar$.

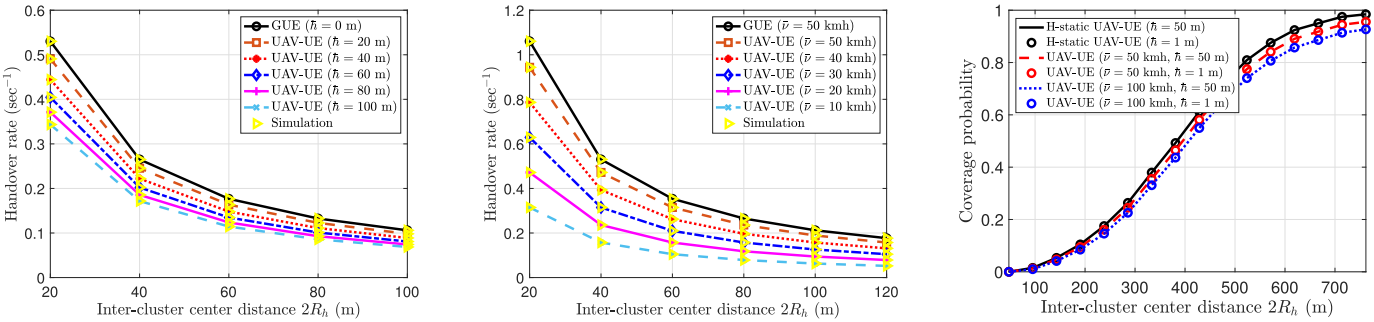


(a) $\bar{\nu} = 30\,\text{kmh}$, $\mu = 300\,\text{km}^{-2}$ (b) $\mu = 100\,\text{km}^{-2}$, $\hbar = 50\,\text{m}$ (c) $\mu = 100\,\text{km}^{-2}$, $\beta = 1$

Fig. 9. Effect of the 3D mobility on the performance of aerial and ground UEs when they are served via CoMP transmission with the inter-cluster center distance set equal to $2R_h$. In (c), H-static refers to an UAV-UE that only moves in the vertical direction within an altitude difference $\hbar$.

TABLE III

CHANNEL MODEL FOR URBAN-MICRO WITH UAV-UES [31] AND [49]

| Channel Model | Description |
|---|---|
| Channel fading | Table. B-2 in [31] |
| Probability of LoS | Table. B-1 in [31] |
| Shadowing effect | Log-normal (standard deviation from Table. B-3 in [31]) |
| System bandwidth | 10 MHz [49] |
| Thermal noise and frequency | $-174$ dBm/Hz power spectral density, 700 MHz [49] |
| Channel estimation | Known CSI |

as $\bar{\nu}$ increases, which corresponds to a higher handover rate (penalized by $\beta$). This slight decrease is essentially because as the inter-cluster distance becomes larger, the probability of handover decreases and its effect gradually vanishes. Similar to the nearest association scheme, the altitude difference $\hbar$ has a minor effect on the coverage probability of UAV-UEs. In addition to its impact on the coverage probability, the mobility of UAV-UEs can decrease their throughput, particularly, when accounting for the handover execution time [48].

Finally, we compare the obtained upper and lower bounds on the coverage probability with the results based on measurements and system level simulations that are found in [31] and [49]. We consider a system setup whose channel parameter values are indicated in Table. III. For a fair comparison, we consider a cooperative transmission scheme from nearest BSs within a collaboration distance $R_c$ according to the proposed deployment of ground BSs, whose parameter values are from Table. II. In particular, Fig. 10 plots the UAV-UE

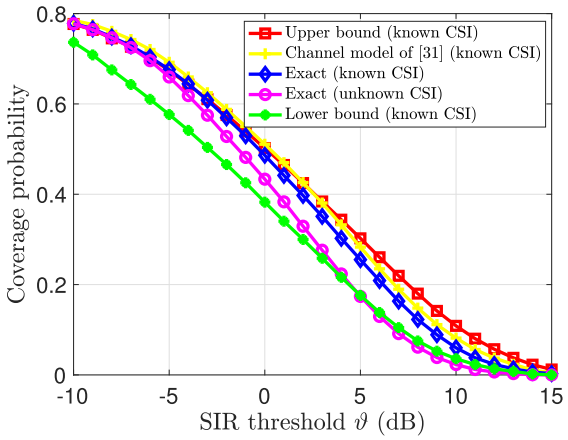


Fig. 10. Comparison of the UAV-UE coverage probability under different setups and assumptions. Specifically, the proposed mathematical model is evaluated versus the channel models of [31] and [49], and also assessed for known and unknown CSI.

coverage probability versus the SIR threshold $\vartheta$ resulting from the proposed channel models of [31] and [49]. From Fig. 10, we can see that the proposed mathematical model gives a performance that is relatively close to the system evaluations based on the channel models of [31] and [49]. Fig. 10 also shows that the UAV-UE coverage probability under the assumption of known CSI at the serving BSs surpasses that of the non-coherent transmission (i.e., unknown CSI).

## VII. Conclusion

In this paper, we have proposed a novel framework for cooperative transmission that can be leveraged to provide reliable connectivity and omnipresent mobility support for UAV-UEs. In order to analytically characterize the performance of UAV-UEs, we have employed Cauchy's inequality and moment approximation of Gamma RVs to derive upper and lower bounds on the UAV-UE coverage probability. Moreover, we have developed a novel 3D RWP model that allowed us to explore the role of UAV-UEs' mobility in cellular networks, particularly, to quantify the handover rate and the impact of their mobility on the achievable performance. For both static and mobile UAV-UEs, we have shown allowing CoMP transmission significantly improves the achievable coverage probability, e.g., from $28\%$ for the baseline scenario with nearest serving BSs, to $60\%$ for static UAV-UEs. Furthermore, comparing the performance of UAV-UEs to ground UEs, it is shown that the coverage probability of a UAV-UE is always upper bounded by that of a ground UE owing to the down-tilted antenna pattern and LoS-dominated interference for UAV-UEs. Our results for the case of mobile UAV-UEs have also revealed that their handover rate and handover probability decrease as the altitude difference increases, i.e., in the case of frequent up and down motions of the UAV-UEs along their trajectory. Moreover, while the altitude difference has a minor effect on the coverage probability of mobile UAV-UEs, their speed noticeably degrades their coverage probability. Finally, the analysis of multiple trajectories under various mobility constraints is an important extension for our future work.

## Appendix A
## Proof of Theorem 1

We proceed to obtain an UB on the coverage probability as follows:

$$\begin{aligned}
&\mathbb{P}\Big(\frac{\kappa P_t J}{I_{\text{out}}} > \vartheta\Big) \\
&= \mathbb{P}\Big(\kappa P_t J > \vartheta I_{\text{out}}\Big) \\
&= \mathbb{E}_{I_{\text{out}}}\Big[\mathbb{P}\Big(\kappa P_t J > \vartheta I_{\text{out}}\Big)\Big] \\
&\overset{(a)}{\approx} \mathbb{E}_{I_{\text{out}}}\Big[\sum_{i=0}^{K-1} \frac{(\vartheta/\kappa P_t\theta)^i}{i!} I_{\text{out}}^i \exp\Big(-\frac{\vartheta}{\kappa P_t\theta} I_{\text{out}}\Big)\Big] \\
&\overset{(b)}{=} \mathbb{E}_{I_{\text{out}}}\Big[\sum_{i=0}^{K-1} \frac{(-\varpi)^i}{i!} \frac{d^i}{d\varpi^i} \mathcal{L}_{I_{\text{out}}|\boldsymbol{r}_\kappa}(\varpi)\Big], \qquad (30)
\end{aligned}$$

where (a) follows from the PDF of Gamma RV whose shape and scale parameters are $\theta$ from (6), and $K = m_l\kappa$, respectively. (b) follows from $\varpi = \frac{\vartheta}{\kappa P_t\theta}$, along with the Laplace transform of interference, i.e., the RV $I_{\text{out}}$. Next, we derive the Laplace transform of interference:

$$\begin{aligned}
&\mathcal{L}_{I_{\text{out}}|\boldsymbol{r}_\kappa}(\varpi) \\
&= \mathbb{E}_{I_{\text{out}}}\Big[e^{-\varpi I_{\text{out}}}\Big] \\
&= \mathbb{E}\Bigg[e^{-\sum_{j\in\Phi_b\setminus\mathcal{B}(0,R_c)} \varpi\chi_j P(u_j)^2}\Bigg] \\
&= \mathbb{E}_{\Phi_b,\chi_j}\Bigg[\prod_{j\in\Phi_b\setminus\mathcal{B}(0,R_c)} e^{-\varpi\chi_j P(u_j)^2}\Bigg] \\
&\overset{(a)}{=} \exp\Bigg(-2\pi\lambda_b \int_{\upsilon=R_c}^{\infty} \Big(1 - \mathbb{E}_\chi e^{-\varpi\chi P(\upsilon)^2}\Big)\upsilon \mathrm{d}\upsilon\Bigg) \qquad (31) \\
&\overset{(b)}{=} \exp\Bigg(-2\pi\lambda_b \int_{\upsilon=R_c}^{\infty} \Big(1 - \delta_l\mathbb{P}_l(\upsilon) - \delta_n\mathbb{P}_n(\upsilon)\Big)\upsilon \mathrm{d}\upsilon\Bigg) \\
&\overset{(c)}{=} e^{\Omega(\varpi)_{|\boldsymbol{r}_\kappa}}, \qquad (32)
\end{aligned}$$

where $\delta_l = \Big(1 + \frac{\varpi P_l(\upsilon)^2}{m_l}\Big)^{-m_l}$, and $\delta_n = \Big(1 + \frac{\varpi P_n(\upsilon)^2}{m_n}\Big)^{-m_n}$; (a) follows from the probability generating functional (PGFL) of PPP along with Cartesian to polar coordinates conversion [34], (b) follows from the moments of the Gamma RV $\chi \sim \text{Gamma}(m_v, 1/m_v)$ modeling the interfering channel gain, and (c) follows from $\Omega(\varpi)_{|\boldsymbol{r}_\kappa} = -2\pi\lambda_b \int_{\upsilon=R_c}^{\infty} \Big(1 - \delta_l\mathbb{P}_l(\upsilon) - \delta_n\mathbb{P}_n(\upsilon)\Big)\upsilon \mathrm{d}\upsilon$. In [37], it is proved that $\sum_{i=0}^{K-1} \frac{(-\varpi)^i}{i!}\mathcal{L}^{(i)}_{I|\boldsymbol{r}_\kappa}(\varpi) = \sum_{i=0}^{K-1} p_i$, where $p_i = \frac{(-\varpi)^i}{i!}\mathcal{L}^{(i)}_{I|\boldsymbol{r}_\kappa}(\varpi)$ can be computed from the recursive relation: $p_i = \sum_{l=0}^{i-1} \frac{i-l}{i} p_l t_{i-l}$, with $t_{i-1} = \frac{(-\varpi)^{i-1}}{(i-1)!}\Omega^{(i-1)}(\varpi)$, and $\Omega^{(i-1)}(\varpi) = \frac{d^{i-1}}{d\varpi^{i-1}}\Omega(\varpi)_{|\boldsymbol{r}_\kappa}$. After some algebraic manipulation as in [37], $\mathbb{P}^l_{\text{c}|\boldsymbol{r}}$ can be expressed in a compact form $\mathbb{P}^l_{\text{c}|\boldsymbol{r}} = \|e^{\boldsymbol{T}_k}\|_1$, where $\|.\|_1$ represents the induced $\ell_1$ norm, and $\boldsymbol{T}_K$ is the lower triangular Toeplitz matrix whose entries are $t_i$, $i = |\{1, \ldots, K\}$. This completes the proof.

## Appendix B
## Proof of Corollary 1

We first write the exponent power of (31) as

$$\begin{aligned}
\Omega(\varpi)_{|\boldsymbol{r}_\kappa} &= -2\pi\lambda_b\mathbb{E}_\chi \int_{\upsilon=R_c}^{\infty} \big(1 - e^{-\varpi\chi P(\upsilon)^2}\big)\upsilon \mathrm{d}\upsilon \\
&\overset{(a)}{=} -2\pi\lambda_b\mathbb{E}_\chi \int_{\upsilon=R_c}^{\infty} \big(1 - e^{-\varpi\varsigma\chi(\upsilon^2+h^2)^{-\alpha_l/2}}\big)\upsilon \mathrm{d}\upsilon,
\end{aligned}$$

where (a) follows from $P(\upsilon)^2 = P_t A_l G_s \big(\upsilon^2 + h^2\big)^{-\alpha_l/2}$ and substituting $\varsigma = P_t A_l G_s$. Let $g = \upsilon^2 + h^2$, and $\mathrm{d}g = 2\upsilon \mathrm{d}\upsilon$, we hence get

$$\Omega(\varpi)_{|\boldsymbol{r}_\kappa} = -\pi\lambda_b\mathbb{E}_\chi \int_{g=R_c^2+h^2}^{\infty} \big(1 - e^{-\varpi\varsigma\chi g^{-\alpha_l/2}}\big)\mathrm{d}g. \qquad (33)$$

By changing the variables $y = g^{-\alpha_l/2}$, $g = y^{-2/\alpha_l}$, and $\mathrm{d}g = \frac{-2}{\alpha_l} y^{\frac{-2}{\alpha_l}-1}\mathrm{d}y$, and solving the reproduced integrals as in [50], we get $\Omega(\varpi)_{|\boldsymbol{r}_\kappa} =$

$$\begin{aligned}
&\pi\lambda_b R_{ch}^2 - \delta_l\pi\lambda_b(\varpi\varsigma)^{\delta_l}\mathbb{E}_\chi\Big[\chi^{\delta_l}\gamma(-\delta_l, \varpi\varsigma\chi R_{ch}^{-\alpha_l/2})\Big] \\
&\overset{(a)}{=} \pi\lambda_b R_{ch}^2 - \delta_l\pi\lambda_b(\varpi\varsigma)^{\delta_l} \\
&\quad \mathbb{E}_\chi\Big[\chi^{\delta_l}\epsilon_1 F_1(-\delta_l; 1-\delta_l; -\varpi\varsigma\chi R_{ch}^{-\alpha_l/2})\Big], \qquad (34)
\end{aligned}$$

where $R_{ch}^2 = R_c^2 + h^2$, $\delta_l = \frac{2}{\alpha_l}$, $\epsilon = \frac{(\varpi\varsigma\chi)^{-\delta_l} R_{ch}^2}{\delta_l}$, and $\gamma(s, x) = \int_0^x t^{s-1}e^{-t}$ is the lower incomplete Gamma function; (a) follows from ${}_1F_1(s; s+1; -x) = \frac{s}{x^s}\gamma(s, x)$,

where ${}_1F_1(\cdot;\cdot;\cdot)$ is the confluent hypergeometric function of the first kind. By rearranging (34), we can obtain $\Omega(\varpi)_{|\boldsymbol{r}_\kappa}$

$$= \pi\lambda_b R_{ch}^2\left(1-\mathbb{E}_\chi\left[{}_1F_1(-\delta_l;1-\delta_l;-\varpi\varsigma\chi R_{ch}^{-\alpha_l/2})\right]\right). \quad (35)$$

The non-zero terms in $\boldsymbol{T}_k$ can be then determined from:

$$\begin{aligned}
t_k &= \frac{(-\varpi)^k}{k!}\Omega(\varpi)^{(k)}_{|\boldsymbol{r}_\kappa} = \pi\lambda_b R_{ch}^2\frac{(-\varpi)^k}{k!}\\
&\quad\times\frac{d^k}{d\varpi^k}\left[1-\mathbb{E}_\chi\left[{}_1\ F_1(-\delta_l;1-\delta_l;-\varpi\varsigma\chi R_{ch}^{-\alpha_l/2})\right]\right]\\
&= \pi\lambda_b R_{ch}^2\mathbb{E}_\chi\left[\frac{(-\varpi)^k}{k!}(-\varsigma\chi R_{ch}^{-\alpha_l/2})^k\right.\\
&\quad\left.\times\frac{d^k}{d(-\varpi\varsigma\chi R_{ch}^{-\alpha_l/2})^k}\left[1-{}_1\ F_1(-\delta_l;1-\delta_l;-\varpi\varsigma\chi R_{ch}^{-\alpha_l/2})\right]\right]\\
&= \pi\lambda_b R_{ch}^2\mathbb{E}_\chi\left[\frac{(\varpi\varsigma\chi R_{ch}^{-\alpha_l/2})^k}{k!}\right.\\
&\quad\left.\times\frac{d^k}{d(-\varpi\varsigma\chi R_{ch}^{-\alpha_l/2})^k}\left[1-{}_1\ F_1(-\delta_l;1-\delta_l;-\varpi\varsigma\chi R_{ch}^{-\alpha_l/2})\right]\right]\\
&\overset{(b)}{=} \pi\lambda_b R_{ch}^2\left(\mathbf{1}\{k=0\}-\frac{(\varpi\varsigma R_{ch}^{-\alpha_l/2})^k}{\Gamma(k+1)}\frac{\delta_l}{(\delta_l-k)}\right.\\
&\quad\left.\times\mathbb{E}_\chi\left[\chi^k{}_1F_1(k-\delta_l;k+1-\delta_l;-\varpi\varsigma\chi R_{ch}^{-\alpha_l/2})\right]\right), \quad (36)
\end{aligned}$$

where (b) follows from the derivatives for hypergeometric functions: $\frac{d^k}{dz^k}{}_1\ F_1(a;b;z)=\frac{\prod_{p=0}^{k-1}(a+p)}{\prod_{p=0}^{k-1}(b+p)}\times{}_1\ F_1(a+k;b+k;z)$. By letting $a_k=(\varpi\varsigma R_{ch}^{-\alpha_l/2})^k$, we get

$$\begin{aligned}
t_k &= \pi\lambda_b R_{ch}^2\left(\mathbf{1}\{k=0\}-\frac{\delta_l a_k}{(\delta_l-k)\Gamma(k+1)}\right.\\
&\quad\left.\times\mathbb{E}_\chi\left[\chi^k{}_1F_1(k-\delta_l;k+1-\delta_l;-\varpi\varsigma\chi R_{ch}^{-\alpha_l/2})\right]\right). \quad (37)
\end{aligned}$$

Lastly, to get a closed-form expression for $t_k$, we average over $\chi\sim\text{Gamma}(m_l,1/m_l)$ as follows:

$$\begin{aligned}
t_k &= \pi\lambda_b R_{ch}^2\left(\mathbf{1}\{k=0\}-b_k\int_{\chi=0}^{\infty}\chi^{k+m_l-1}e^{-m_l\chi}\right.\\
&\quad\left.\times{}_1F_1(k-\delta_l;k+1-\delta_l;-\varpi\varsigma R_{ch}^{-\alpha_l/2}\chi)\mathrm{d}\chi\right)\\
&= \pi\lambda_b R_{ch}^2\left(\mathbf{1}\{k=0\}-b_k\Gamma(k+m_l)m_l^{-(k+m_l)}\right.\\
&\quad\left.\times{}_2F_1(k+m_l,k-\delta_l;k+1-\delta_l;-\varpi\varsigma R_{ch}^{-\alpha_l/2}m_l)\right)\\
&\overset{(c)}{=} \pi\lambda_b R_{ch}^2\Big(\mathbf{1}\{k=0\}\\
&\quad-c_{k2}F_1(k+m_l,k-\delta_l;k+1-\delta_l;-\varpi\varsigma R_{ch}^{-\alpha_l/2}m_l)\Big), \quad (38)
\end{aligned}$$

where $b_k=\frac{\delta_l a_k m_l^{m_l}}{(\delta_l-k)\Gamma(k+1)\Gamma(m_l)}$, $c_k=\frac{m_l^{m_l}}{\Gamma(m_l)}b_k=\frac{\delta_l a_k\Gamma(k+m_l)m_l^{-k}}{(\delta_l-k)\Gamma(k+1)\Gamma(m_l)}$, and (c) follows from solving the integral in (38) [51, Eq. 7.525] and rearranging the right hand side. This completes the proof.

## Appendix C
## Proof of Lemma 2

When $\varphi_t=0$, the conditional probability of handover can be expressed as

$$\begin{aligned}
&\mathbb{P}(H|r_0)\\
&= 1-\mathbb{E}_{\rho_t,Z_t,Z_{t-1}}\left[e^{-\pi\lambda_b\left((\bar\nu\cos(\varphi_t))^2+2r_0\bar\nu\cos(\varphi_t)\right)}\right] \quad (39)\\
&\overset{(a)}{\le} 1-\underbrace{e^{-\pi\lambda_b\mathbb{E}_{\rho_t,Z_t,Z_{t-1}}\left(\frac{2r_0\bar\nu\varrho_t}{\sqrt{\varrho_t^2+(z_t-z_{t-1})^2}}+(\frac{\bar\nu\varrho_t}{\sqrt{\varrho_t^2+(z_t-z_{t-1})^2}})^2\right)}}_{\mathbb{P}(\bar H|r_0)}, \quad (40)
\end{aligned}$$

where (a) follows from Jensen's inequality, which implies that $\mathbb{E}[e^{-x}]\ge e^{\mathbb{E}[-x]}$ as $e^{-x}$ is a convex function of $x$. $\mathbb{P}(\bar H|r_0)$ is an LB on the probability of no handover conditioned on $r_0$. We obtain $\mathbb{P}(\bar H|r_0)$, shown at the bottom of this page, in (40), where (b) follows from averaging over $\rho_t$ whose PDF is $f_{\rho_t}(\varrho_t)$. By changing the variables: $p=z_t-z_{t-1}$, with $f_P(p)=\frac{\hbar-|p|}{\hbar^2},\forall-\hbar\le p\le\hbar$, we get, (41) and (42), shown at the top of the next page, where $(c)$ follows from solving the left integral of (41) [51, Section 7.8], and the substitution

$$\begin{aligned}
\zeta(\mu,\hbar) &= \frac{\pi\mu\bar\nu^2}{\hbar^2}\int_{-\hbar}^{\hbar}(\hbar-|p|)\big(\frac{1}{\pi\mu}-p^2e^{\pi\mu p^2}\Gamma\left(0,\pi p^2\mu\right)\big)\mathrm{d}p\\
&= \bar\nu^2-\frac{\pi\mu\bar\nu^2}{\hbar^2}\int_{-\hbar}^{\hbar}(\hbar-|p|)p^2e^{\pi\mu p^2}\Gamma\left(0,\pi p^2\mu\right)\mathrm{d}p\\
&\overset{(d)}{=} \bar\nu^2-\frac{2\pi\mu\bar\nu^2}{\hbar^2}\int_0^{\hbar}(\hbar-p)p^2e^{\pi\mu p^2}\Gamma\left(0,\pi p^2\mu\right)\mathrm{d}p. \quad (43)
\end{aligned}$$

where (d) follows from the symmetry of the integrand. From (42) and (43), with the fact that $\mathbb{P}(H|r_0)=1-\mathbb{P}(\bar H|r_0)$, the proof is completed.

## Appendix D
## Proof of Proposition 1

Following the Buffon's needle approach for hexagonal cells [46], we have

$$\mathbb{E}[N]=\frac{4\sqrt{3}}{3\pi\ell}\mathbb{E}[V_h]\mathbb{E}[T]=\frac{2}{\pi R_h}\mathbb{E}[V_h]\mathbb{E}[T], \quad (44)$$

$$\begin{aligned}
\mathbb{P}(\bar H|r_0) &= e^{-\pi\lambda_b\mathbb{E}_{\rho_t,Z_t,Z_{t-1}}\left(\frac{2r_0\bar\nu\varrho_t}{\sqrt{\varrho_t^2+(z_t-z_{t-1})^2}}+(\frac{\bar\nu\varrho_t}{\sqrt{\varrho_t^2+(z_t-z_{t-1})^2}})^2\right)}\\
&\overset{(b)}{=} e^{-\pi\lambda_b\mathbb{E}_{Z_t,Z_{t-1}}\left[r_0\sqrt{\pi}\bar\nu_1F_1\left(\frac12;0;\pi(z_t-z_{t-1})^2\mu\right)\right]}e^{-\pi\lambda_b\mathbb{E}_{Z_t,Z_{t-1}}\left[\pi\mu\bar\nu^2\left(\frac{1}{\pi\mu}-(z_t-z_{t-1})^2e^{\pi\mu(z_t-z_{t-1})^2}\Gamma\left(0,\pi(z_t-z_{t-1})^2\mu\right)\right)\right]}
\end{aligned}$$

$$\mathbb{P}(\bar{H}|r_0) \;=\; e^{-\frac{\pi\lambda_b r_0\sqrt{\pi\bar{\nu}}}{\hbar^2}\int_{-\hbar}^{\hbar}(\hbar-|p|)_1F_1\left(\frac{1}{2};0;\pi p^2\mu\right)\mathrm{d}p} e^{-\frac{\pi\lambda_b\pi\mu\bar{\nu}^2}{\hbar^2}\int_{-\hbar}^{\hbar}(\hbar-|p|)\left(\frac{1}{\pi\mu}-p^2e^{\pi\mu p^2}\Gamma\left(0,\pi p^2\mu\right)\right)\mathrm{d}p} \tag{41}$$

$$\overset{(c)}{=}\; e^{-\frac{2\pi\lambda_b r_0\sqrt{\pi\bar{\nu}}}{\hbar^2}\left(\frac{\pi\hbar^2\mu G_{2,3}^{2,2}\left(\hbar^2\pi\mu\middle|\begin{matrix}\frac{1}{2},\frac{1}{2}\\0,1,-\frac{1}{2}\end{matrix}\right)-G_{2,3}^{2,2}\left(\hbar^2\pi\mu\middle|\begin{matrix}1,\frac{3}{2}\\1,2,0\end{matrix}\right)}{\pi^2\mu}\right)}e^{-\pi\lambda_b\zeta(\mu,\hbar)}, \tag{42}$$

where $\mathbb{E}[V_h]$ represents the average horizontal speed of the UAV-UE. Given the constant speed assumption, $\mathbb{E}[V_h] = \bar{\nu}\mathbb{E}[\cos(\varphi_t)]$, where $\varphi_t = \arccos\left(\frac{\varrho_t}{\sqrt{\varrho_t^2+(z_t-z_{t-1})^2}}\right)$. We hence have

$$\mathbb{E}[V_h] \;=\; \mathbb{E}_{\rho_t,Z_t,Z_{t-1}}\left[\frac{\bar{\nu}\varrho_t}{\sqrt{\varrho_t^2+(z_t-z_{t-1})^2}}\right]$$
$$\overset{(a)}{=}\; \frac{\sqrt{\pi}\bar{\nu}}{2}\mathbb{E}_{Z_t,Z_{t-1}}\left[{}_1F_1\left(\frac{1}{2};0;\pi(z_t-z_{t-1})^2\mu\right)\right] \tag{45}$$

where (a) follows from averaging over the RV $\rho_t$. By proceeding similar to Appendix C to obtain $\mathbb{E}[V_h]$, the handover rate can be obtained from $H = \frac{\mathbb{E}[N]}{\mathbb{E}[T]}$. This completes the proof.

## REFERENCES


[1] R. Amer, W. Saad, H. ElSawy, M. M. Butt, and N. Marchetti, "Caching to the sky: Performance analysis of cache-assisted CoMP for cellular-connected UAVs," in *Proc. IEEE Wireless Commun. Netw. Conf. (WCNC)*, Apr. 2019, pp. 1–6.

[2] M. Vondra, M. Ozger, D. Schupke, and C. Cavdar, "Integration of satellite and aerial communications for heterogeneous flying vehicles," *IEEE Netw.*, vol. 32, no. 5, pp. 62–69, Sep. 2018.

[3] W. Saad, M. Bennis, and M. Chen, "A vision of 6G wireless systems: Applications, trends, technologies, and open research problems," *IEEE Netw.*, to be published.

[4] M. Mozaffari, W. Saad, M. Bennis, Y.-H. Nam, and M. Debbah, "A tutorial on UAVs for wireless networks: Applications, challenges, and open problems," *IEEE Commun. Surveys Tuts.*, vol. 21, no. 3, pp. 2334–2360, 3rd Quart., 2019.

[5] M. Mozaffari, A. Taleb Zadeh Kasgari, W. Saad, M. Bennis, and M. Debbah, "Beyond 5G with UAVs: Foundations of a 3D wireless cellular network," *IEEE Trans. Wireless Commun.*, vol. 18, no. 1, pp. 357–372, Jan. 2019.

[6] Y. Zeng, Q. Wu, and R. Zhang, "Accessing from the sky: A tutorial on UAV communications for 5G and beyond," 2019, *arXiv:1903.05289*. [Online]. Available: http://arxiv.org/abs/1903.05289

[7] Y. Zeng, J. Lyu, and R. Zhang, "Cellular-connected UAV: Potential, challenges, and promising technologies," *IEEE Wireless Commun.*, vol. 26, no. 1, pp. 120–127, Feb. 2019.

[8] *Unmanned Aircraft Systems—Trial Report*, LTE Qualcomm, San Diego, CA, USA, 2017.

[9] X. Lin *et al.*, "The sky is not the limit: LTE for unmanned aerial vehicles," *IEEE Commun. Mag.*, vol. 56, no. 4, pp. 204–210, Apr. 2018.

[10] B. V. Der Bergh, A. Chiumento, and S. Pollin, "LTE in the sky: Trading off propagation benefits with interference costs for aerial nodes," *IEEE Commun. Mag.*, vol. 54, no. 5, pp. 44–50, May 2016.

[11] M. M. Azari, F. Rosas, A. Chiumento, and S. Pollin, "Coexistence of terrestrial and aerial users in cellular networks," in *Proc. IEEE Globecom Workshops (GC Wkshps)*, Singapore, Dec. 2017, pp. 1–6.

[12] R. Amer, W. Saad, and N. Marchetti, "Toward a connected sky: Performance of beamforming with down-tilted antennas for ground and UAV user co-existence," *IEEE Commun. Lett.*, vol. 23, no. 10, pp. 1840–1844, Oct. 2019.

[13] C. D'Andrea, A. Garcia-Rodriguez, G. Geraci, L. Galati Giordano, and S. Buzzi, "Cell-free massive MIMO for UAV communications," 2019, *arXiv:1902.03578*. [Online]. Available: http://arxiv.org/abs/1902.03578

[14] A. Rahmati, Y. Yapıcı, N. Rupasinghe, I. Guvenc, H. Dai, and A. Bhuyany, "Energy efficiency of RSMA and NOMA in cellular-connected mmWave UAV networks," 2019, *arXiv:1902.04721*. [Online]. Available: http://arxiv.org/abs/1902.04721

[15] N. Cherif, M. Alzenad, H. Yanikomeroglu, and A. Yongacoglu, "Downlink coverage and rate analysis of an aerial user in integrated aerial and terrestrial networks," 2019, *arXiv:1905.11934*. [Online]. Available: http://arxiv.org/abs/1905.11934

[16] L. Liu, S. Zhang, and R. Zhang, "Multi-beam UAV communication in cellular uplink: Cooperative interference cancellation and sum-rate maximization," *IEEE Trans. Wireless Commun.*, vol. 18, no. 10, pp. 4679–4691, Oct. 2019.

[17] W. Mei, Q. Wu, and R. Zhang, "Cellular-connected UAV: Uplink association, power control and interference coordination," *IEEE Trans. Wireless Commun.*, vol. 18, no. 11, pp. 5380–5393, Nov. 2019.

[18] L. Liu, S. Zhang, and R. Zhang, "CoMP in the sky: UAV placement and movement optimization for multi-user communications," *IEEE Trans. Commun.*, vol. 67, no. 8, pp. 5645–5658, Aug. 2019.

[19] S. Zhang, Y. Zeng, and R. Zhang, "Cellular-enabled UAV communication: A connectivity-constrained trajectory optimization perspective," *IEEE Trans. Commun.*, vol. 67, no. 3, pp. 2580–2604, Mar. 2019.

[20] S. Zhang and R. Zhang, "Trajectory design for cellular-connected UAV under outage duration constraint," 2019, *arXiv:1901.04286*. [Online]. Available: http://arxiv.org/abs/1901.04286

[21] U. Challita, W. Saad, and C. Bettstetter, "Interference management for cellular-connected UAVs: A deep reinforcement learning approach," *IEEE Trans. Wireless Commun.*, vol. 18, no. 4, pp. 2125–2140, Apr. 2019.

[22] P. K. Sharma and D. I. Kim, "Coverage probability of 3-D mobile UAV networks," *IEEE Wireless Commun. Lett.*, vol. 8, no. 1, pp. 97–100, Feb. 2019.

[23] P. K. Sharma and D. I. Kim, "Random 3D mobile UAV networks: Mobility modeling and coverage probability," *IEEE Trans. Wireless Commun.*, vol. 18, no. 5, pp. 2527–2538, May 2019.

[24] S. Enayati, H. Saeedi, H. Pishro-Nik, and H. Yanikomeroglu, "Moving aerial base station networks: A stochastic geometry analysis and design perspective," *IEEE Trans. Wireless Commun.*, vol. 18, no. 6, pp. 2977–2988, Jun. 2019.

[25] M. Banagar and H. S. Dhillon, "Performance characterization of canonical mobility models in drone cellular networks," *IEEE Trans. Wireless Commun.*, to be published.

[26] M. M. Azari, F. Rosas, and S. Pollin, "Cellular connectivity for UAVs: Network modeling, performance analysis, and design guidelines," *IEEE Trans. Wireless Commun.*, vol. 18, no. 7, pp. 3366–3381, Jul. 2019.

[27] S. Euler, H.-L. Maattanen, X. Lin, Z. Zou, M. Bergström, and J. Sedin, "Mobility support for cellular connected unmanned aerial vehicles: Performance and analysis," in *Proc. IEEE Wireless Commun. Netw. Conf. (WCNC)*, Marrakesh, Morocco, Apr. 2019, pp. 1–6.

[28] A. Fakhreddine, C. Bettstetter, S. Hayat, R. Muzaffar, and D. Emini, "Handover challenges for cellular-connected drones," in *Proc. ACM Workshop Micro Aerial Vehicle Netw., Syst., Appl.*, New York, NY, USA, 2019, pp. 9–14.

[29] M. Ding, P. Wang, D. Lopez-Perez, G. Mao, and Z. Lin, "Performance impact of LoS and NLoS transmissions in dense cellular networks," *IEEE Trans. Wireless Commun.*, vol. 15, no. 3, pp. 2365–2380, Mar. 2016.

[30] B. Galkin, J. Kibilda, and L. A. DaSilva, "A stochastic model for UAV networks positioned above demand Hotspots in urban environments," *IEEE Trans. Veh. Technol.*, vol. 68, no. 7, pp. 6985–6996, Jul. 2019.

[31] *Technical Specification Group Radio Access Network; Study on Enhanced LTE Support for Aerial Vehicles*, document G. T. 36.777, Dec. 2017.

[32] R. Austin, *Unmanned Aircraft Systems: UAVS Design, Development and Deployment*, vol. 54. Hoboken, NJ, USA: Wiley, 2011.

[33] Z. Chen, J. Lee, T. Q. S. Quek, and M. Kountouris, "Cooperative caching and transmission design in cluster-centric small cell networks," *IEEE Trans. Wireless Commun.*, vol. 16, no. 5, pp. 3401–3415, May 2017.

[34] M. Haenggi, *Stochastic Geometry for Wireless Networks*. Cambridge, U.K.: Cambridge Univ. Press, 2012.

[35] G. Nigam, P. Minero, and M. Haenggi, "Coordinated multipoint joint transmission in heterogeneous networks," *IEEE Trans. Commun.*, vol. 62, no. 11, pp. 4134–4146, Nov. 2014.

[36] R. W. Heath, Jr., T. Wu, Y. H. Kwon, and A. C. K. Soong, "Multiuser MIMO in distributed antenna systems with out-of-cell interference," *IEEE Trans. Signal Process.*, vol. 59, no. 10, pp. 4885–4899, Oct. 2011.

[37] X. Yu, C. Li, J. Zhang, M. Haenggi, and K. B. Letaief, "A unified framework for the tractable analysis of multi-antenna wireless networks," *IEEE Trans. Wireless Commun.*, vol. 17, no. 12, pp. 7965–7980, Dec. 2018.

[38] C. Bettstetter, G. Resta, and P. Santi, "The node distribution of the random waypoint mobility model for wireless ad hoc networks," *IEEE Trans. Mobile Comput.*, vol. 2, no. 3, pp. 257–269, Jul. 2003.

[39] C. Bettstetter, H. Hartenstein, and X. Pérez-Costa, "Stochastic properties of the random waypoint mobility model," *Wireless Netw.*, vol. 10, no. 5, pp. 555–567, Sep. 2004.

[40] E. Hyytia, P. Lassila, and J. Virtamo, "Spatial node distribution of the random waypoint mobility model with applications," *IEEE Trans. Mobile Comput.*, vol. 5, no. 6, pp. 680–694, Jun. 2006.

[41] X. Lin, R. K. Ganti, P. J. Fleming, and J. G. Andrews, "Towards understanding the fundamentals of mobility in cellular networks," *IEEE Trans. Wireless Commun.*, vol. 12, no. 4, pp. 1686–1698, Apr. 2013.

[42] M. J. Neely and E. Modiano, "Capacity and delay tradeoffs for ad hoc mobile networks," *IEEE Trans. Inf. Theory*, vol. 51, no. 6, pp. 1917–1937, Jun. 2005.

[43] R. Amer, W. Saad, B. Galkin, and N. Marchetti, "Performance analysis of mobile cellular-connected drones under practical antenna configurations," in *Proc. IEEE Int. Conf. Commun. (ICC)*, Dublin, Ireland, Jun. 2020, pp. 1–8.

[44] P. K. Sharma and D. I. Kim, "Coverage probability of 3D UAV networks with RWP mobility-based altitude control," in *Proc. IEEE Int. Conf. Commun. Workshops (ICC Workshops)*, May 2018, pp. 1–6.

[45] X. Xu, Z. Sun, X. Dai, T. Svensson, and X. Tao, "Modeling and analyzing the cross-tier handover in heterogeneous networks," *IEEE Trans. Wireless Commun.*, vol. 16, no. 12, pp. 7859–7869, Dec. 2017.

[46] H. Tabassum, M. Salehi, and E. Hossain, "Mobility-aware analysis of 5G and B5G cellular networks: A tutorial," 2018, *arXiv:1805.02719*. [Online]. Available: http://arxiv.org/abs/1805.02719

[47] S. Sadr and R. S. Adve, "Handoff rate and coverage analysis in multi-tier heterogeneous networks," *IEEE Trans. Wireless Commun.*, vol. 14, no. 5, pp. 2626–2638, May 2015.

[48] R. Arshad, H. ElSawy, S. Sorour, T. Y. Al-Naffouri, and M.-S. Alouini, "Velocity-aware handover management in two-tier cellular networks," *IEEE Trans. Wireless Commun.*, vol. 16, no. 3, pp. 1851–1867, Mar. 2017.

[49] G. Geraci, A. Garcia-Rodriguez, L. Galati Giordano, D. Lopez-Perez, and E. Bjornson, "Understanding UAV cellular communications: From existing networks to massive MIMO," *IEEE Access*, vol. 6, pp. 67853–67865, 2018.

[50] J. G. Andrews, F. Baccelli, and R. K. Ganti, "A tractable approach to coverage and rate in cellular networks," *IEEE Trans. Commun.*, vol. 59, no. 11, pp. 3122–3134, Nov. 2011.

[51] I. S. Gradshteyn and I. M. Ryzhik, *Table of Integrals, Series, and Products*. New York, NY, USA: Academic, 2014.


**Ramy Amer** (Student Member, IEEE) received the M.Sc. degree in electrical engineering from Alexandria University, Egypt, in 2016. He is currently pursuing the Ph.D. degree in wireless communication, especially, wireless caching, with CONNECT Centre, Trinity College Dublin, Ireland, under the supervision of Dr. Nicola Marchetti. His research interests include cross-layer design, cognitive radio, energy harvesting, stochastic geometry, and reinforcement learning. Prior to CONNECT, he was also an Assistant Lecturer for Switching Department, National Telecommunication Institute of Egypt (NTI), Cairo, Egypt, where he conducted professional training both at the national and international levels. He was a Visiting Scholar at Wireless, Virginia Tech, under Prof. Walid Saad's Group from September 2018 to March 2019. He was a recipient of Best Paper Award from IFIP NTMS in 2019 and the IEEE Student Travel Grant from IEEE WCNC in 2019. He was also a recipient of the Exemplary Reviewer recognition from the IEEE TRANSACTIONS ON COMMUNICATIONS in 2019. He is also certified as a Cisco instructor and has other Cisco data and voice certificates. He worked as a part-time instructor for many national and international training centres such as New-Horizon Egypt and Fast-Lane KSA.

**Walid Saad** (Fellow, IEEE) received the Ph.D. degree from the University of Oslo in 2010. He is currently a Professor with the Department of Electrical and Computer Engineering, Virginia Tech, where he leads the Network sciEnce, Wireless, and Security (NEWS) Laboratory. His research interests include wireless networks, machine learning, game theory, security, unmanned aerial vehicles, cyber-physical systems, and network science. He is also a recipient of the NSF CAREER Award in 2013, the AFOSR Summer Faculty Fellowship in 2014, and the Young Investigator Award from the Office of Naval Research (ONR) in 2015. He was the author/coauthor of eight conference best paper awards at WiOpt in 2009, ICIMP in 2010, IEEE WCNC in 2012, IEEE PIMRC in 2015, IEEE SmartGridComm in 2015, EuCNC in 2017, IEEE GLOBECOM in 2018, and IFIP NTMS in 2019. He is was recipient of the 2015 Fred W. Ellersick Prize from the IEEE Communications Society, the 2017 IEEE ComSoc Best Young Professional in Academia Award, the 2018 IEEE ComSoc Radio Communications Committee Early Achievement Award, and the 2019 IEEE ComSoc Communication Theory Technical Committee. From 2015 to 2017, he was named the Stephen O. Lane Junior Faculty Fellow at Virginia Tech. In 2017, he was named the College of Engineering Faculty Fellow. He received the Dean's award for Research Excellence from Virginia Tech in 2019. He currently serves as an Editor for IEEE TRANSACTIONS ON WIRELESS COMMUNICATIONS, IEEE TRANSACTIONS ON MOBILE COMPUTING, and IEEE TRANSACTIONS ON COGNITIVE COMMUNICATIONS AND NETWORKING. He is an Editor-at-Large of IEEE TRANSACTIONS ON COMMUNICATIONS. He is an IEEE Distinguished Lecturer.

**Nicola Marchetti** (Senior Member, IEEE) received the Ph.D. degree in wireless communications from Aalborg University, Denmark, in 2007, the M.Sc. degree in electronic engineering from the University of Ferrara, Italy, in 2003, and the M.Sc. degree in mathematics from Aalborg University in 2010. He is currently an Assistant Professor in wireless communications with Trinity College Dublin, Ireland. He performs his research under the Trinity Information and Complexity Labs (TRICKLE) and the Irish Research Centre for Future Networks and Communications (CONNECT). His collaborations include research projects in cooperation with Nokia Bell Labs and US Air Force Office of Scientific Research, among others. He has authored 130 journals and conference papers, two books and eight book chapters, holds three patents, and received four best paper awards. His research interests include adaptive and self-organizing networks, complex systems science for communication networks, PHY layer, and radio resource management.